High Performance Piezoelectric MEMS Microphones

by

Robert John Littrell

A dissertation submitted in partial fulfillment
of the requirements for the degree of
Doctor of Philosophy
(Mechanical Engineering)
in The University of Michigan
2010

Doctoral Committee:

Professor Karl Grosh, Chair
Professor David R. Dowling
Professor Khalil Najafi
Assistant Professor Kenn Richard Oldham

TABLE OF CONTENTS

LIST OF FIGURES

Figure

LIST OF TABLES

Table

LIST OF ABBREVIATIONS

AlN aluminum nitride

AFM atomic force microscope

Ar argon

ASIC application specific integrated circuit

dBA A-weighted decibel scale

BOE buffered oxide etch

CMOS complimentary metal oxide semiconductor

DRIE deep reactive ion etching

FET field effect transistor

FWHM full width half maximum

H_2O water

HCl hyrdochloric acid

HNO_3 nitric acid

IEEE Institute of Electrical and Electronics Engineers

JFET junction field effect transistor

LCR inductance-capacitance-resistance

LNF Lurie Nanofabrication Facility

Mo molybdenum

MEMS microelectromechanical systems

N_2 nitrogen

PCB printed circuit board

PECVD plasma enhanced chemical vapor deposition

P(VDF-TrFE) piezoelectric copolymer of polyvinylidene flouride

PZT lead zirconate titanate

p-JFET P-type junction field effect transistor

RMS root mean square

SPC small piezoelectric coupling

SPL sound pressure level

THD total harmonic distortion

TMAH tetramethylammonium hydroxide

TO transistor outline

XRD X-ray diffraction

ZnO zinc oxide

LIST OF SYMBOLS

a acceleration

A_c, A_e, A_s cross-sectional, electrode, sensor area

A_n, A_m, A_0 Fourier Series coefficient

b beam width

c speed of sound in air

$\mathbf{c}$ 6 x 6 stiffness matrix

C electrical capacitance

C_{front}, C_t, C_{back} acoustic compliance

C_1, C_2 constants of integration

$\mathbf{d}$ 3 x 6 piezoelectric coupling coefficient matrix

d_{31} element of the piezoelectric coupling coefficient matrix

D electric displacement

$\mathcal{D}$ diaphragm flexural rigidity

$\mathbf{D}$ 3 x 1 electric displacement vector

$\mathbf{e}$ 3 x 6 piezoelectric coupling coefficient matrix

E electric field

$\mathbf{E}$ 3 x 1 electric field vector

f frequency

F force

g gap width

g_{fs} transistor transconductance

h layer height

i layer index

i_g, i_d small signal current noise

I area moment of inertia

I_G, I_Q large signal current

I_0, I_1 modified bessel function

j square root of -1

J_0, J_1 bessel function

k wave number

k_B Boltzmann constant

l gap length

L beam length

L_{front}, L_t acoustic inductance

M moment

$\overline{MV}$ piezoelectric induced moment

n layer index

N total number of layers

$\mathcal{N}$ diaphragm tension per unit length

p_z pressure in the z-direction

P peak amplitude of a harmonic pressure

q electron charge

r radial coordinate

R acoustic, electrical, or mechanical resistance

$\mathcal{R}$ diaphragm radius

R_r radiation resistance

R_f dielectric film equivalent series resistance

R_L load resistance

R_{front}, R_t, R_{back} acoustic resistance

s, s_{11} element of the compliance matrix

$\mathbf{s}$ 6 x 6 compliance matrix

T diaphragm tension per unit area

T_k temperature

v voltage

V voltage

$\forall$ volume

V_{TO} threshold voltage

w diaphragm displacement; beam displacement

x cartesian coordinate

y cartesian coordinate

Y Young's modulus

YI beam flexural rigidity

$\overline{YI}$ beam flexural rigidity without assuming SPC

z cartesian coordinate

zm_i distance to the middle of layer i

zn distance to the neutral axis

Z_{Qi} SPC constant

Z_{Ci} SPC constant

$\alpha, \alpha_1, \alpha_2$ SPC constant, diaphragm constant

β beam constant

γ diaphragm constant

δ material loss angle

ϵ electric permittivity

$\boldsymbol{\epsilon}$ 3 x 3 electric permittivity matrix

ε strain

$\boldsymbol{\varepsilon}$ 6 x 1 strain vector

θ azimuthal coordinate

κ tension parameter

λ SPC constant

Λ SPC constant

ν Poisson's ratio

ξ loss angle calculation constant

ρ density

σ stress

$\boldsymbol{\sigma}$ 6 x 1 stress matrix

ς conductivity

ϕ electric potential

Ψ optimization parameter

ω radian frequency

CHAPTER I

Introduction

Microphones are used in a variety of everyday devices such as telephones and computers but also have many specialized applications such as studio recording and laboratory testing. Every year, more than two billion microphones are built for a range of applications. Most of these microphones convert sound into an electrical signal by utilizing capacitive transduction. Piezoelectric transduction, however, offers unique advantages over capacitive transduction such as simplicity of fabrication and linearity. These advantages have led to a further investigation of the typically cited disadvantages of piezoelectric technology such as noise floor and sensitivity. Microphones utilizing piezoelectric transduction have been designed, fabricated, and tested. This work has led to new models of piezoelectric cantilevers and more accurate methods for determining appropriate model assumptions. New, more accurate, methods of determining piezoelectric coupling coefficients have been developed. Optimization techniques which apply to a broad range of piezoelectric sensors have been identified. Piezoelectric microphone advantages and limitations will be demonstrated.

1.1 Capacitive and Piezoelectric MEMS Microphones

Microelectromechanical systems (MEMS) is a term used to describe a variety of electro-mechanical devices built by utilizing equipment and techniques originally de-

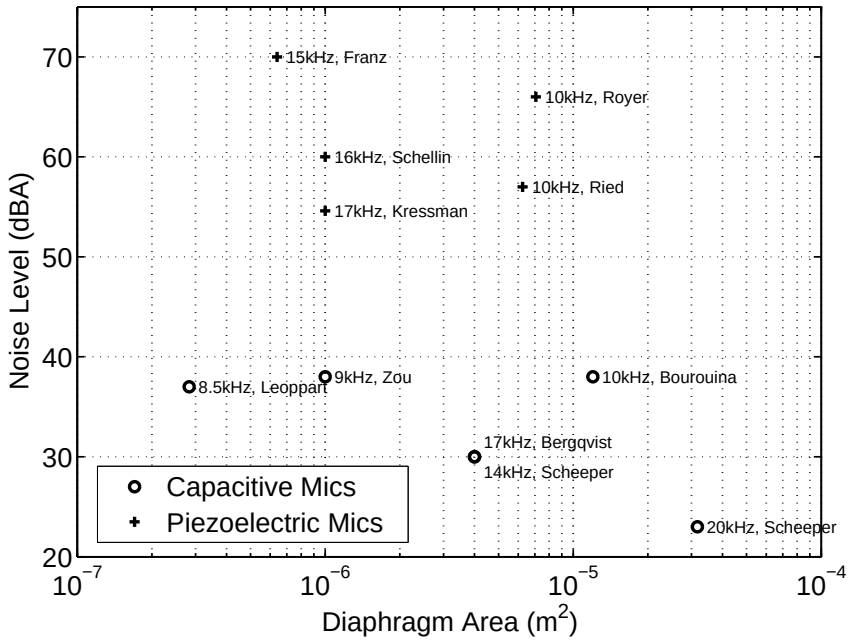

Figure 1.1: Capacitive and piezoelectric microphone noise levels as of December 2009.

veloped for integrated circuit manufacturing. These techniques, therefore, allow for mechanical devices with very small, well defined features to be built. Since the early 1980's, researchers have been developing MEMS microphones that utilize both capacitive and piezoelectric transduction [1, 2]. Typically, MEMS piezoelectric microphones have had a much higher noise floor (>10×) than capacitive microphones as seen in Figure 1.1. This large disparity between capacitive and piezoelectric performance has contributed to the adoption of capacitive transduction as the dominant technique for MEMS microphones. Today, millions of capacitive MEMS microphones are built each year.

The basic parameters of concern for any microphone, regardless of sensing technique, are input referred noise (also measured as minimum detectable signal, signal-to-noise ratio, or noise floor), total harmonic distortion (THD, also measured as maximum input level or dynamic range), and bandwidth (also measured as resonant frequency). Also of interest are factors such as sensitivity, power consumption,

cost, and output impedance but these will not be stressed as heavily in the following work because they are not inherent limitations of the device itself. For example, the sensitivity of any microphone can be increased (without significant change in input referred noise, bandwidth, or distortion) by adding an appropriate amplifier to an existing microphone. Likewise, the power consumption of capacitive and piezoelectric microphones is more a function of their amplifying electronics than of the specific devices. It is, however, important to evaluate the total microphone/amplifier (or preamplifier) system because the system output must be such that it can be sensed, amplified, or buffered without affecting any of the basic parameters of concern.

1.2 Noise

Noise is referred to as the inherent system fluctuations in system inputs or outputs such as voltage, current, pressure, and displacement. This is separate from interference from external signals because this interference is not an inherent limitation as it can be removed. This work will primarily be concerned with thermal noise. Thermal noise (also referred to as Johnson noise) was first documented by Johnson in 1928 [3]. Johnson noticed an electromotive force in conductors that is related to their temperature. Nyquist then explained these results as a consequence of Brownian motion [4, 5]. The theory of Nyquist was proved by Callen and Welton in 1951 [6]. Callen and Welton also gave examples of mechanical systems that exhibit noise resulting from mechanical dissipation [6]. Simply, any mechanism that converts mechanical or electrical energy to thermal energy, such as a resistor or damper, also converts thermal energy to mechanical or electrical energy. Therefore, any dissipative system at a temperature above absolute zero will have noise associated with random thermal agitation.

In a microphone/amplifier system, each significant noise source must be taken into account. To do this, the effect of each noise source can be traced through the system

to the output. The noise on the output is referred to as output referred noise. The sensitivity of the device (for a microphone this is given in V/Pa) can then be used to determine the equivalent noise at the input called the input referred noise. This input referred noise is ultimately the noise of interest in any sensing system. Input referred microphone noise is typically quoted as a sound pressure level (SPL) given on an A-weighted scale (dBA). The A-weighted scale weights specific frequencies to mimic the sensitivity of human hearing. The noise level is then converted to SPL, a decibel scale referenced to 20 μPa, the nominal lower limit of human hearing.

The noise floor of capacitive microphones is typically limited by noise in the microphone itself, the microphone preamplifier, or both. The dominant noise source in the microphone is thermal noise resulting from damping seen by air entering and leaving the small capacitive gap between the diaphragm and backplate [7]. The microphone preamplifier noise is determined by the circuitry and can be affected by the device capacitance, depending on the amplification scheme used [8, 9].

As a simplified example of capacitive microphone optimization, consider a MEMS microphone consisting of a diaphragm and backplate. The backplate has holes to reduce the resistance to air escaping the gap, thereby reducing the noise in the microphone. If the microphone noise is dominant over the preamplifier noise, the number of holes in the backplate can be increased or the distance between the backplate and the diaphragm can be increased, both of which reduce air flow resistance and, therefore, microphone noise [8]. Both of these changes also reduce the microphone capacitance and sensitivity, thereby increasing the input referred preamplifier noise [8]. It is beneficial to reduce the microphone noise at the expense of preamplifier noise until the preamplifier noise becomes larger than the microphone noise. At the point where both contribute equally to the overall noise of interest, the total microphone noise has been minimized. This general microphone optimization technique can be used for any capacitive microphone, MEMS or otherwise.

Although several groups have developed piezoelectric MEMS microphones, the fundamental limiting factor for noise floor remains unclear. Typical piezoelectric microphones consist of multiple sensing electrodes due to the varying stress in piezoelectric material on a diaphragm [1, 10, 11, 12, 13]. Researchers have exploited the fact that these electrodes can be combined to trade off sensitivity for device capacitance [10, 11]. When combined optimally, the combination of electrodes will preserve the total output energy of the piezoelectric device but the capacitance can be adjusted to minimize the effect of circuit noise on the microphone [10]. This method of minimizing noise, however, neglects all noise coming from the piezoelectric microphone and only minimizes the circuit noise.

The piezoelectric microphone will have thermal noise that stems from radiation resistance [14] as well as structural damping [8]. The device will also have thermal noise caused by the real part of the electrical impedance of the piezoelectric material as described by Levinzon in a paper addressing piezoelectric accelerometers [15]. This noise is determined by the loss angle (or dissipation factor) of the material and will be filtered by the capacitance of the device [15]. Depending on the piezoelectric material and amplification scheme used, this noise can be the dominant noise source and cannot be ignored. This work will present complete microphone/amplifier system noise models. This work will also present optimization techniques for reducing the noise floor of piezoelectric devices. The noise models will be validated experimentally.

1.3 Sensitivity

Microphone sensitivity is also of importance because this sensitivity is used to map electrical noise back to the input. Piezoelectric microphone sensitivities ranging from 85 μV/Pa [13] to 920 μV/Pa [10] have been reported with typical values around 200 μV/Pa [1, 11, 12]. Microphone sensitivity can be modeled by using a variety of piezoelectric laminate models that have been under development since the

discovery of piezoelectric materials more than 100 years ago by the brothers Curie [5]. A piezoelectric material is one that becomes electrically polarized when strained (called the direct piezoelectric effect) and conversely, becomes strained when placed in an electric field (called the converse piezoelectric effect) [16]. A sensor such as a microphone utilizes the direct piezoelectric effect but it is not always appropriate to ignore the strain resulting from the converse piezoelectric effect. The converse piezoelectric effect can also be used to build actuators or measure piezoelectric coupling coefficients [17].

The Institute of Electrical and Electronics Engineers (IEEE) has released a standard on piezoelectricity [18]. This standard lists the piezoelectric constitutive equations as

$$\boldsymbol{\sigma} = \mathbf{c}^{\mathbf{E}}\boldsymbol{\varepsilon} - \mathbf{e}^{\mathbf{t}}\mathbf{E} \tag{1.1}$$

$$\mathbf{D} = \mathbf{e}\boldsymbol{\varepsilon} - \epsilon^{\boldsymbol{\varepsilon}}\mathbf{E} \tag{1.2}$$

where $\boldsymbol{\sigma}$ is the 6×1 stress vector, $\mathbf{c}^{\mathbf{E}}$ is the 6×6 stiffness matrix measured under zero electric field, $\boldsymbol{\varepsilon}$ is the 6×1 strain vector, $\mathbf{e}$ is the 3×6 piezoelectric coupling coefficient matrix, $\mathbf{E}$ is the 3×1 electric field vector, $\mathbf{D}$ is the 3×1 electric displacement vector, and $\epsilon^{\boldsymbol{\varepsilon}}$ is the 3×3 electric permittivity matrix measured under zero strain. Equation 1.1 is similar to Hooke's law but includes an additional term which couples the mechanical and electrical domains. Equation 1.2 is similar to the definition of electric displacement but includes an additional term coupling the mechanical and electrical domains. This coupling between mechanical and electrical domains means that a complete model of a piezoelectric material must include Equations 1.1 and 1.2 in some form. Often, however, if the piezoelectric material is used for actuation (converse piezoelectric effect), Equation 1.2 is ignored [19]. If the piezoelectric material is used as a sensor (direct piezoelectric effect), the electric field term is often ignored in

Equation 1.1 and the electric field and electric displacement can be computed using Equation 1.2 and the electrical boundary conditions [20]. *Small piezoelectric coupling* (SPC) is the term given to these two assumptions [21].

Several piezoelectric materials of interest such as aluminum nitride (AlN), zinc oxide (ZnO), and lead zirconate titanate (PZT) belong to the dihexagonal polar class of crystals (6 mm). Many models assume the piezoelectric crystal is of this class because these materials are common and this assumption simplifies Equations 1 and 2. Microphones of this class are characterized by a piezoelectric coupling coefficient matrix of the form

$$d = \begin{bmatrix} 0 & 0 & 0 & 0 & d_{15} & 0 \\ 0 & 0 & 0 & d_{15} & 0 & 0 \\ d_{31} & d_{31} & d_{33} & 0 & 0 & 0 \end{bmatrix}$$

and a compliance matrix of the form

$$s = \begin{bmatrix} s_{11} & s_{12} & s_{13} & 0 & 0 & 0 \\ s_{12} & s_{11} & s_{13} & 0 & 0 & 0 \\ s_{13} & s_{13} & s_{33} & 0 & 0 & 0 \\ 0 & 0 & 0 & s_{14} & 0 & 0 \\ 0 & 0 & 0 & 0 & s_{14} & 0 \\ 0 & 0 & 0 & 0 & 0 & 2(s_{11} - s_{12}) \end{bmatrix}$$

These forms are most convenient for the strain-charge form of the piezoelectric constitutive equations given in Chapter II. The form of the stiffness matrix, $\mathbf{c}$, and the piezoelectric coupling matrix, $\mathbf{e}$, are the same as $\mathbf{s}$ and $\mathbf{d}$, respectively, except $c_{66} = 1/2(c_{11} - c_{12})$.

Microphones are most easily realized using a diaphragm or cantilever beam [1, 22]. Cantilevers will be the focus of this work because they are free of residual stress while diaphragm stiffness is often dominated by residual stress. This residual stress can

be difficult to predict and control and can lead to degraded device performance [23]. Most models of piezoelectric multilayer beams assume that plane sections remain plane (referred to as the Euler-Bernoulli assumption) [24, 25, 26] while others make the Timoshenko assumption that allows for shear and rotary inertia [27]. This work will focus on beam models utilizing the Euler-Bernoulli assumption because the added accuracy of the Timoshenko assumption is not necessary for the designs and tests of interest.

The assumption of small piezoelectric coupling (SPC) will be investigated. Some have said that SPC can be assumed whenever the piezoelectric coupling coefficient is small [24] while others claim that the SPC assumption can lead to significant errors for structures in which the substrate thickness is similar to or smaller than that of the piezoelectric layer [28]. Criterion for determining the validity of the SPC assumption will be presented in the following work. This work will also present analytical models of multilayer piezoelectric beams both with and without SPC. These models will be used to measure piezoelectric coupling coefficients as well as device sensitivity experimentally in order to validate these models.

1.4 Linearity

The linearity of the microphone/amplifier system can be limited by the microphone, amplifier, or both. Capacitive devices are inherently nonlinear due to the nonlinear relationship between capacitance and gap size. As diaphragm deflection increases, distortion increases so THD at a specific SPL can be decreased by increasing the diaphragm stiffness. In this manner, microphone distortion and bandwidth can be improved at the expense of noise and sensitivity. With the application of appropriate electronics, the capacitive nonlinearity will limit the SPL at which low harmonic distortion is achieved. This tradeoff can be observed by comparing two capacitive microphones, one designed for low noise and one for high dynamic range. The low

noise microphone has a diaphragm area of 2.8×10^{-7} m^2, a noise floor of 37 dBA, and a 1% THD at 100 dB SPL [29]. This A-weighted noise floor would be equivalent to 13 μPa/$\sqrt{Hz}$. The high dynamic range microphone has a diaphragm area of 1.7×10^{-7} m^2, a resonant frequency of 178 kHz, input referred noise of roughly 2.2 mPa/$\sqrt{Hz}$ at 1 kHz, and has linear operation up to 164 dB SPL. The first microphone's input referred noise is roughly 45 dB lower than the second but the second is linear up to a SPL that is roughly 64 dB higher than the first.

Piezoelectric transduction can be assumed to be linear in the presence of small electric fields but becomes nonlinear as the electric fields become large [30]. The nonlinearity of PZT is primarily attributed to its ferroelectric hysteresis [31]. The nonlinearity of non-ferroelectric piezoelectric materials such as ZnO and AlN has also been investigated [32, 33] but well established, experimentally validated nonlinear models of piezoelectric AlN or ZnO have not been found. Experiments performed in the completion of the present work have indicated that AlN remains linear for electric fields in excess of 1×10^6 V/m. The structure can also provide a source of sensor nonlinearity. The primary source of cantilever beam nonlinearity is in the relationship between curvature and displacement. At large deflections, the beam curvature cannot be approximated as the second derivative of the displacement and the deflection is, therefore, a nonlinear function of applied pressure. Although the deflection is not linearly related to applied pressure when deflections are large, the layer stress and therefore the output voltage remains a linear function of applied acoustic pressure. The primary source of diaphragm nonlinearity is due to the stretching of the neutral axis and does result in nonlinear stress in the piezoelectric layers [34].

1.5 Piezoelectric Materials

Piezoelectric material selection can have significant impact on device performance. Different piezoelectric materials exhibit vastly different qualities and it is extremely

important to use the best material to suit a particular application. The most common piezoelectric materials for MEMS devices are ZnO, PZT, and AlN.

ZnO and AlN are quite similar in that they are both dihexagonal polar crystals ($6mm$) and are non-ferroelectric [35, 36]. AlN has the advantage of being compatible with silicon semiconductor technology while ZnO can be problematic. AlN also has a higher resistivity than ZnO. Because it can be difficult to deposit ZnO with a high resistivity, sensors and actuators operating below 10 kHz often require an insulating layer, usually SiO2, to reduce charge leakage [36, 37]. Despite these advantages, ZnO has been used more commonly due to the better availability of ZnO films, less demanding vacuum conditions for ZnO, and some early negative experiences with residual stresses in AlN films. Over the past few years, AlN deposition has become more prevalent and the residual stress has been shown to be more controllable [35, 38].

Both AlN and ZnO are commonly sputter deposited and as such, AlN and ZnO thin films are almost always polycrystalline materials. The piezoelectric coupling coefficients result from the average effect of all crystals. These materials must be deposited in such a manner as to align the crystals or they will exhibit degraded piezoelectric properties. X-ray diffraction is typically used to evaluate the degree of orientation of these materials [36]. X-ray diffraction rocking curves with full width half maximum (FWHM) values below 2° are typically considered well oriented for AlN films [35]. PZT differs from ZnO and AlN in that it is a ferroelectric material. This means that, unlike that of AlN and ZnO, the polar axis of PZT can be reoriented after deposition [36]. PZT has been primarily designed to have high piezoelectric coupling coefficients [36] while relatively little effort has been put into improving its other properties. Some of the most relavent properties of ZnO, PZT, and AlN for this study are shown in Table 1.1 for comparison.

	ZnO	PZT	AlN
d_{31} (C/N)	-5.74×10^{-12} [39]	-40×10^{-12} - -70×10^{-12} [36]	-2.65×10^{-12} [40]
d_{33} (C/N)	10.4×10^{-12} [39]	92×10^{-12}-203×10^{-12} [36]	5.53×10^{-12} [40]
s_{11} (Pa^{-1})	9.63×10^{-12} [39]	9.52×10^{-12}-14.9×10^{-12}[41]	3.53×10^{-12}[40]
$\tan(\delta)$	0.01-0.1 [36]	0.03-0.05 [42]	0.002 [42]
ϵ_{33}/ϵ_o	10.9[36]	1100-1300 [42]	10.4 [42]
ρ (kg/m^3)	5670	7600	3300

Table 1.1: Range of properties of common MEMS piezoelectric materials.

1.6 Capacitive Microphone Embodiments

Figure 1.1 shows, briefly, the performance of several capacitive MEMS microphones. The smallest of these microphones was built by researchers at Knowles Electronics [29]. This microphone has a 600 μm polysilicon diaphragm positioned 4 μm from the backplate. As noted in the paper, film stress significantly impacts the sensitivity of the microphone. If not controlled, variations in film stress will lead to unacceptable variations in microphone sensitivity. For this reason, the diaphragm is left floating with only a single attachment between the silicon wafer and the diaphragm for electrical connection. When in use, an 11 V bias voltage holds the diaphragm 4 μm from the backplate, giving a device capacitance of 0.5 pF. The output is buffered by an application specific integrated circuit (ASIC) resulting in a packaged microphone with a 37 dBA noise floor. As this microphone became a commercial device, it probably represents the most highly optimized capacitive MEMS microphone of those in Figure 1.1.

The microphone built by Bergqvist and Rudolf is another representation of a high performance capacitive microphone [43]. This microphone has a 5 μm thick 2 mm $\times$ 2 mm silicon diaphragm and a 4.5 pF working capacitance. When a 6 V bias was applied, the microphone exhibited a 30 dBA noise floor. This device has a lower noise floor than that described above but a larger area. As the area of a microphone increases, the noise floor would be expected to drop. Because noise combines as the

square root of the sum of the squares and the sensitivity sums, doubling the sensor area should result in a 3 dB improvement in noise floor. This device has roughly 14 times the area of a microphone with a 600 μm diameter and should therefore have a noise floor 11.5 dB lower. This analysis would indicate that this microphone is not as well optimized as the smaller microphone detailed above.

1.7 Piezoelectric Microphone Embodiments

The performance of several piezoelectric microphones has also been illustrated in Figure 1.1. The lowest noise piezoelectric MEMS microphone detailed above is that built by Kressman et. al [11]. This microphone uses a diaphragm design consisting of a 230 nm oxide/nitride diaphragm, aluminum electrodes, and a 4.3 μm thick P(VDF-TrFE) piezoelectric layer. The piezoelectric material is quite thick because it is very compliant relative to the other materials comprising the diaphragm. The stress of the oxide/nitride diaphragm is reported to be greater than 107 MPa. The diaphragm is 1 mm $\times$ 1 mm and has separate middle and outer electrodes due to differences in stress. The signal is buffered with a p-JFET with a gain of 0.85. The microphone has a capacitance of 4 - 8 pF and a sensitivity of 0.21 mV/Pa. A bandwidth of 17 kHz is given but the authors expect the resonant frequency to be around 100 kHz. These microphones have a noise floor of 54.6 dBA. The authors attribute the increased performance of this microphone to the thickness of the piezoelectric material layer but note that this thickness is limited by an eventual reduction in sensitivity due to a reduction in membrane displacement and by the movement of the neutral axis toward the center of the piezoelectric material.

The microphone designed by Ried et al. is also noteworthy [44]. This microphone is built on the same chip as its CMOS circuitry and some of the CMOS layers are used to form the microphone. The microphone has a 2.4 mm $\times$ 2.4 mm diaphragm that consists of a 1.7 μm silicon nitride layer, a 0.4 μm polysilicon bottom electrode,

a 0.2 μm SiO_2 layer, a 0.5 μm ZnO piezoelectric layer, a 0.1 μm SiO2 layer, and a 0.6 μm Al top electrode. The diaphragm is nominally 3.5 μm thick. The stress of the silicon nitride layer is 140 MPa tensile and that of the ZnO is 1 GPa compressive. These layer stresses are designed to cancel and give a relatively stress-free device. The stress in the diaphragm, however, resulted in a resonant frequency of 18.3 kHz instead of the designed 6.6 kHz and a sensitivity of 0.92 mV/Pa instead of the designed 8.9 mV/Pa. The sensitivity of this device is so high because this device has 8 elements wired in series, providing a high sensitivity but a capacitance of only 2.49 pF. This microphone had a 57 dBA noise floor.

1.8 Gaps in the Literature

Although several piezoelectric MEMS microphones have been fabricated and tested, the fundamental tradeoffs and performance limitations have not yet been fully investigated. While only one of the piezoelectric microphones in Figure 1.1 used AlN, the material properties of AlN indicate that it will lead to better microphones than the more commonly used ZnO and PZT when noise floor is of primary concern. Further, as AlN becomes more prevalent and deposition techniques improve, the properties and applications of AlN will also likely improve.

Additionally, while many piezoelectric MEMS microphone publications cited high residual stress as a factor that reduced microphone sensitivity and increased bandwidth [44, 11, 13], none examined the effect of residual stress when considering a design with a fixed bandwidth. Similarly, many designs focused on maximizing the device sensitivity either by making the piezoelectric layer thick [11] or by wiring several electrodes in series [44]. Only the work of Ried [44], however, attempted to minimize the noise by examining the full transducer/amplifier system. Further, none of these works considered noise from the piezoelectric material loss.

Chapter II will present models of both the MEMS transducer and a low noise

amplifier. Noise resulting from material loss will be included. Together, these models will form a complete system model that will be used to identify the important figures of merit for the MEMS transducer design. The MEMS transducer design will then be optimized to minimize the noise floor of a piezoelectric microphone of fixed area and bandwidth. Cantilever and diaphragm designs will be compared.

Chapter III will then present the design, fabrication, and performance of a piezoelectric MEMS microphone built with these models in mind. While the performance of this first microphone did not meet expectations, it validated the models and illuminated certain fabrication difficulties. Chapter IV will then present a new design aimed at overcoming fabrication issues experienced with the first microphone design. This microphone design is unique in many ways. It is the one of only a few piezoelectric MEMS microphones to utilize AlN as the piezoelectric material, uses a cantilever design in order to avoid the detrimental effects of residual stress, has optimized electrode shapes, and has relatively thin layers. This second iteration will be shown to significantly outperform all previously reported piezoelectric MEMS microphones.

CHAPTER II

Modeling

This chapter will cover several models used to predict microphone performance. First, the dominant noise sources in the microphone will be modeled in Section 2.1. These noise sources include those from the transducer as well as those from a common source amplifier used to buffer the microphone output. The following section, Section 2.2 will present models for the sensitivity of cantilever and diaphragm based microphones. Section 2.3 will provide a discussion of microphone linearity. The linearity of the common source amplifier used to buffer the output will be examined as this is expected to be the much more non-linear than the piezoelectric transducer. A model of a high sound pressure level (SPL) test apparatus used to measure microphone distortion will also be presented in this section. These three sections should provide a fundamental understanding of piezoelectric transduction and the associated noise and linearity concerns.

Sections 2.4 and 2.5 give insight into the optimization of the entire microphone. First, Section 2.4 provides a method of separating the transducer optimization from the amplifier optimization so they can be addressed separately. Section 2.5 then shows how to optimize the transducer alone. As noise has been the most significant hindrance to piezoelectric microphone utilization, this is the focus of the optimization. Section 2.6 contains a discussion of the two most common microphone packages.

This was not incorporated into the optimization because the packaging is designed to prevent environmental factors from disrupting microphone performance but should not inhibit performance in any way. The microphone cross-sensitivity to vibration is then briefly discussed in Section 2.7.

2.1 Noise

The noise floor of a piezoelectric sensing system can be limited by the sensor itself, the amplifying electronics, or both. As such, an electromechanical system model is necessary to determine the noise floor of any piezoelectric device. An example of such a model will be provided for a microphone amplified by a common source amplifier utilizing a junction field effect transistor (JFET). A common source amplifier with a JFET has been selected because JFETs are the leading devices for low-noise applications where the signal source impedance is large [45]. The noise floor of such a common source amplifier is similar to that of other, more complex amplification schemes but its simplicity allows for easier identification of noise sources and design tradeoffs.

2.1.1 Microphone Transducer Noise

The microphone element itself has thermal noise associated with radiation resistance, structural dissipation, electrical loss in the piezoelectric material, and electrode resistance. The radiation resistance is a mechanical resistance and, therefore, has a mechanical thermal noise associated with it. The Nyquist relation gives the thermal noise associated with any resistive element as

$$F^2 = 4k_B R T_k \tag{2.1}$$

where F is the root mean square (rms) value of the force spectral density, k_B is Boltzmann's constant, T_k is the temperature in Kelvin, and R is the resistance. When R is electrical resistance, mechanical resistance, or acoustic resistance, F has units of $V/\sqrt{Hz}$, $N/\sqrt{Hz}$, or $Pa/\sqrt{Hz}$, respectively.

2.1.1.1 Radiation Resistance and Damping

The acoustical radiation resistance of a non-baffled circular radiating piston is

$$R_r = \frac{\rho_o c (kA_s)^2}{4\pi} \tag{2.2}$$

where ρ_o is the density of the fluid, c is the speed of sound in the fluid, k is the wave number defined as the radian frequency (ω) divided by the speed of sound, and A_s is the area of the radiating surface [14]. Equation 2.2 applies to circular radiating pistons but can be applied to radiating surfaces of any shape whenever as is the case for most MEMS microphones and pressure sensors operating in the acoustic range in air [46]. Combining equations 2.1 and 2.2 gives the resulting acoustic noise pressure as a function of frequency. For example, the rms spectral density of pressure noise at $1kHz$ using a 500 μm $\times$ 500 μm square radiating surface in air at room temperature (300 K) is 1.35 $\times$ 10^{-8} $Pa/\sqrt{Hz}$ or an SPL of -63.4 dB re 20 μPa using a 1 Hz bin. This will be shown to be negligible compared to other noise sources.

The thermal noise resulting from structural dissipation is also quite low. It has been shown that as beams are miniaturized, air damping is the dominant source of damping at atmospheric pressure [47]. Since a microphone cannot be vacuum encapsulated, thermal noise resulting from structural damping will be ignored.

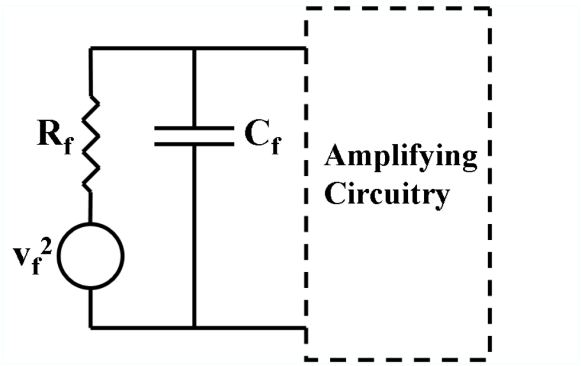

Figure 2.1: Electrical equivalent circuit of piezoelectric sensing element.

2.1.1.2 Material Loss

Electrical noise from the resistance of the piezoelectric material can be calculated using equation 2.1 [15]. The piezoelectric material with electrodes on either side forms a capacitor which can be modeled as capacitance and resistance in parallel as shown in Figure 2.1. The resistance of a film as a function of frequency is

$$R_f = \frac{1}{\omega C_f \tan\delta} \tag{2.3}$$

where C_f is the film capacitance and $\tan\delta$ is the loss angle. The loss angle is the tangent of the angle by which the current in a lossy capacitor lags the current in an ideal capacitor [48]. The loss angle is also referred to as the dissipation factor or the dielectric loss. This loss angle can be used to determine the sensor resistance which can be plugged into equation 2.1 to get a voltage noise spectral density. This voltage noise source is modeled in series with the resistor as shown in Figure 2.1.

2.1.1.3 Electrode Loss

As will be shown, thin electrodes are desirable for high performance. As the electrodes become thin, however, they contribute to the device noise floor so it is important to approximate the impact of thinning electrodes. In order to simulate the effect of thinning electrodes, it is important to capture two separate effects. First, as

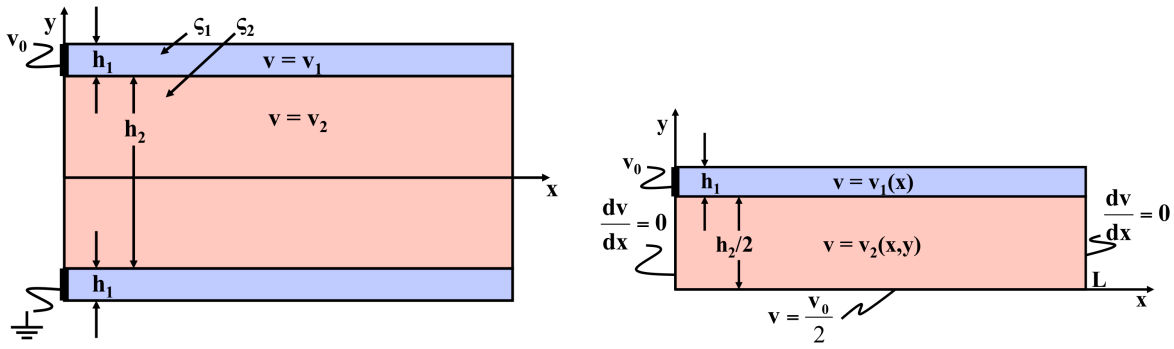

(a) Material stack and variables.

(b) Material stack and boundary conditions

Figure 2.2: Diagram of electrode/dielectric/electrode stack modeled as a continuous system and associated boundary conditions.

the electrode becomes thin, the electrode material resistivity will increase. This has been described and modeled by Namba [49]. Secondly, as the electrode becomes thin, its resistance will increase because the cross-section of the electrode has decreased. This can be investigated by modeling a single layer of the piezoelectric material sandwiched by two electrode layers as a continuous system. A diagram of the continuous system can be seen in Figure 2.2(a). The electrode material, material 1, will be modeled as a conductor with finite, real conductivity, ς_1 and the piezoelectric material will be modeled as a dielectric with complex conductivity given as $\varsigma_2 = \epsilon_o\omega(\tan\delta + j)$. Because the electrode is much longer than it is thick and has a much larger conductivity than the dielectric, the electrode potential is assumed to be constant in the thickness direction and vary only along the length of the beam. Laplace's equation is assumed to hold in the dielectric because the dielectric has very few free charges. These assumptions result in a 1-D model of the conductor coupled to a 2-D model of the dielectric. Figure 2.2(b) illustrates the geometry and assumed boundary conditions.

Solving this problem for voltage gives

$$v_2 = A_o y + \sum_{n=1}^{\infty} A_n \cos\left(\frac{n\pi x}{L}\right) \sinh\left(\frac{n\pi y}{L}\right) + \frac{v_o}{2} \tag{2.4}$$

with

$$A_o = \frac{\int_0^L v_1(x)dx}{Lh_2} \tag{2.5}$$

and

$$A_n = \frac{\int_0^L v_1(x)\cos\left(\frac{n\pi x}{L}\right)dx}{L\sinh\left(\frac{n\pi h_2}{2L}\right)} \tag{2.6}$$

where v_1 and v_2 are the voltages in the conductor and dielectric respectively, v_0 is the applied voltage, h_2 is the height of the dielectric, and L is the length of the beam. The solution for the voltage in the electrode is

$$v_1 = -\frac{\varsigma_2}{\varsigma_1 h_1}\int\int \frac{dv_2(x, y = h_2/2)}{dy}dxdx + C_1(x = L)x + C_2(x = 0) \tag{2.7}$$

where

$$C_1 = \frac{\varsigma_2}{\varsigma_1 h_1}\int \frac{dv_2(x, y = h_2/2)}{dy}dx \tag{2.8}$$

and

$$C_2 = v_o + \frac{\varsigma_2}{\varsigma_1 h_1}\int\int \frac{dv_2(x, y = h_2/2)}{dy}dxdx \tag{2.9}$$

As can be seen, the equations are coupled together and the problem can be solved numerically by guessing a value of v_1, solving for v_2, calculating the new v_1, and iterating until the solution converges. A sample solution with $\varsigma_1 = 1 \times 10^7\ \Omega^{-1}m^{-1}$, $\varsigma_2 = 1\ \Omega^{-1}m^{-1}$, L = 400 μm, h_1 = 10 nm, and h_2 = 1 μm is shown in Figure 2.3.

Only the voltage in the top half of the electrode/material stack is shown due to symmetry. While the values used to create Figure 2.3 show significant voltage loss across the length of the top electrode, realistic values for conductors and dielectrics of interest would show almost no change in voltage across this electrode. Therefore, the problem can be simplified by recognizing that the slope of the voltage in the x-direction will be much less than that in the y-direction and can be ignored. When the slope of the voltage in the x-direction is ignored, instead of using Laplace's equation

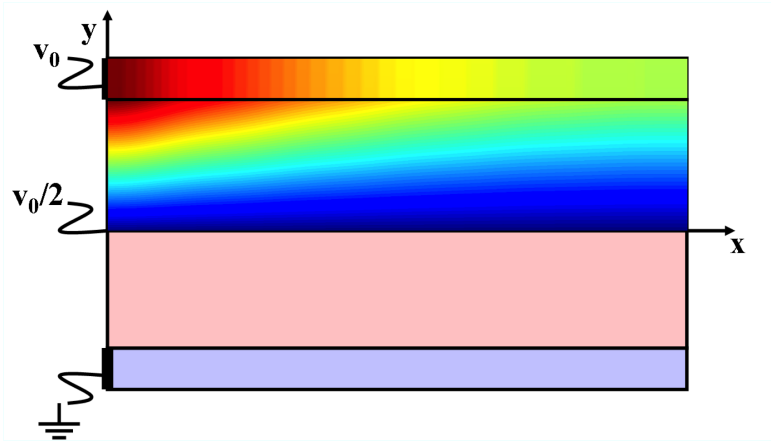

Figure 2.3: The voltage in the material stack varies from the applied voltage (v_0) at the base of the electrode to half of that value at the center of the stack. Only the top half of the stack is shown due to symmetry.

in the dielectric, one can use the equation

$$\frac{d^2 v_2}{dy^2} = 0 \tag{2.10}$$

The voltage in the dielectric then becomes

$$v_2(x, y) = v_1(x)\Big(\frac{y}{h_2} + \frac{1}{2}\Big) \tag{2.11}$$

and that in the conductor is

$$v_1(x) = \frac{v_o}{2}\Big[\cosh\Big(\sqrt{\frac{2\varsigma_2}{\varsigma_1 h_1 h_2}}x\Big) - \tanh\Big(\sqrt{\frac{2\varsigma_2}{\varsigma_1 h_1 h_2}}L\Big)\sinh\Big(\sqrt{\frac{2\varsigma_2}{\varsigma_1 h_1 h_2}}x\Big)\Big] + \frac{v_o}{2}. \tag{2.12}$$

In order to determine the effect on the noise, the effective increase in loss angle must be determined. First, the impedance is determined by dividing the applied voltage by the current into the conductor (as the current into the conductor is equal to the total current through the device),

$$z = \frac{2}{\varsigma_1 h_1 b \xi \tanh(\xi L)} \tag{2.13}$$

where z is the impedance, b is the beam width, and

$$\xi = \sqrt{\frac{2\varsigma_2}{\varsigma_1 h_1 h_2}} \tag{2.14}$$

In equation 2.43, the conductivity of material two, ς_2, is complex which makes the impedance complex. The loss angle is then found by dividing the real part of the impedance by the imaginary part of the impedance. However, this quotient has no closed form solution because the real and imaginary parts of the impedance cannot be separated analytically. The impedance is therefore approximated using a Laurent series for the $1/\tanh(\xi L)$ term leading to a loss angle of

$$\tan(\delta)_{total} = \tan(\delta)_{piezo} + \frac{2\epsilon_o \omega L^2}{3\varsigma_1 h_1 h_2} \tag{2.15}$$

This expression for the total loss angle (that which includes losses in the electrodes) can be substituted into equation 2.3 when calculating overall noise.

2.1.2 Microphone Circuitry Noise

The circuitry, in this case a common source amplifier, will be modeled in a manner consistent with the literature [45]. This model will include thermal noise from the bias resistor, thermal noise in the channel of the JFET, thermal noise from the load resistor, and shot noise in the gate. A model of this circuit can be seen in Figure 2.4. A small signal model with all these noise sources can be seen in Figure 2.5. The thermal noise from resistors R_b and R_L can be computed using equation 2.1. The rms spectral density of the current noise, i_g, can be computed as

$$i_g^2 = 2qI_G \tag{2.16}$$

where q is the electron charge (1.6×10^{-19} C) and I_G is the DC gate current. This noise is similar to quantization error and is caused by the fact that current is carried in discrete quantities. The channel noise, i_d^2, is thermal noise and can be computed as

$$i_d^2 = 4k_B T_k \frac{2}{3} g_{fs} \tag{2.17}$$

where g_{fs} is the JFET transconductance. This noise is caused by the resistance of the channel where the 2/3 factor is typically used for long channel devices [50]. In

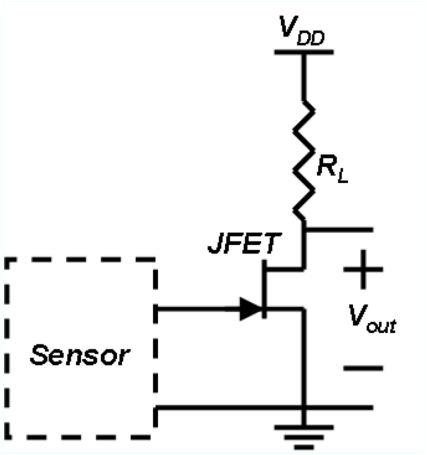

Figure 2.4: Common source amplifier circuit schematic.

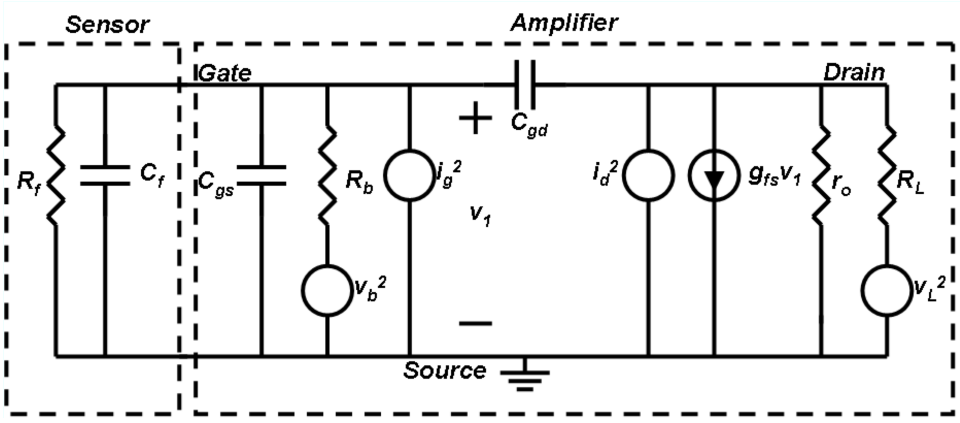

Figure 2.5: Small signal model of the common source amplifier with noise sources.

order to compute the effect of each of these noise sources, all other noise sources are

removed (current sources are open and voltage sources are shorted) and its effect on the output voltage is computed. Each noise source is then combined as the square root of the sum of the squares. The output noise using an n-channel JFET (2sk3719) with a 2.2 kΩ load resistor, a sensor capacitance of 10 pF, and a 3 V V_{DD} can be seen in Figure 2.6. Each individual noise source as well as the total summation of noise can be seen in the figure. The sensor resistance has been ignored in this drawing.

The thermal noise from the bias resistor, R_b, is filtered by the combined capacitance of the sensor and the gate source capacitance as seen in Figure 2.6. Therefore, as the sensor capacitance increases, the output noise from the bias resistor is reduced. This will be an important relationship as the sensor/amplifier system is optimized.

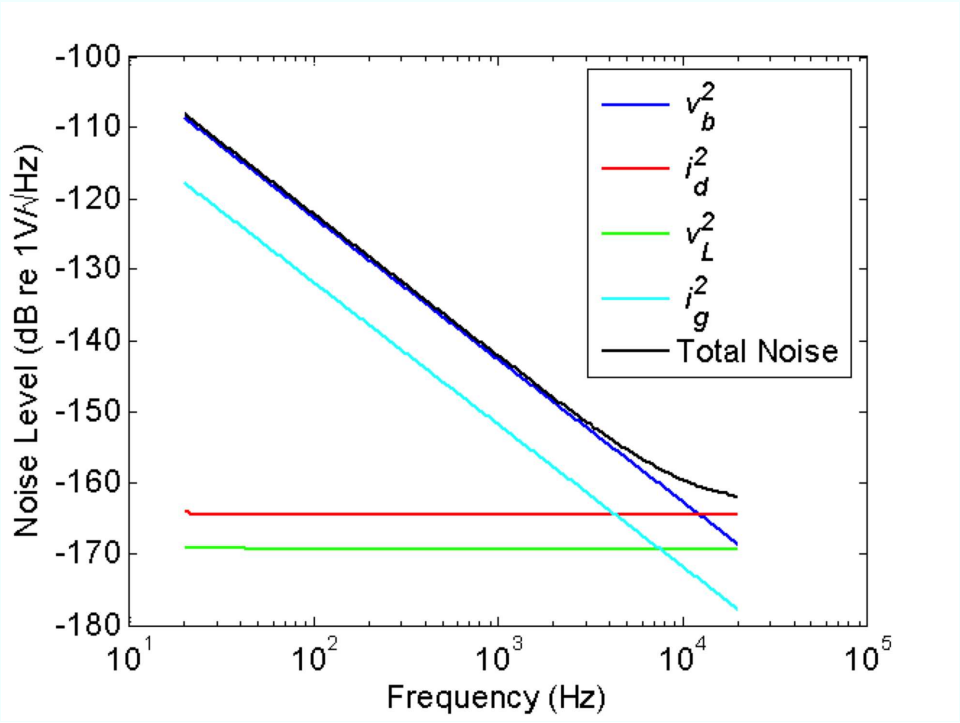

Figure 2.6: Output noise of common source amplifier. Plot includes noise from the bias resistor, shot noise, channel noise, and noise from the load resistor.

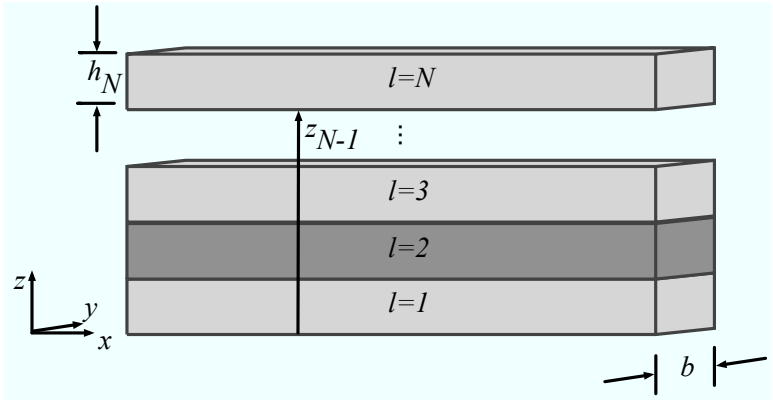

Figure 2.7: Piezoelectric laminate beam layer numbering and orientation.

2.2 Sensitivity

Many of the noise calculations in the last chapter provide an output noise in volts. This noise is only relevant when related to the input via the microphone sensitivity. This section will focus on multi-layer cantilevers of uniform width and electrodes along their entire length as shown in Figure 2.7. These cantilevers will be used to determine piezoelectric coupling coefficients of films and to sense acoustic pressure. Most piezoelectric microphones use either a diaphragm or cantilever design. A cantilever is a good choice because it is free from residual stress which has been shown to significantly reduce the sensitivity of diaphragm-based microphones. Following an in depth cantilever sensitivity derivation, the sensitivity of a diaphragm based piezoelectric sensor will also be presented.

2.2.1 Cantilever Transducer Sensitivity

For this analysis, it is more convenient to use the piezoelectric coupling equations in the strain charge form written as

$$\boldsymbol{\varepsilon} = \mathbf{s_E}\boldsymbol{\sigma} + \mathbf{d}^{\mathbf{t}}\mathbf{E} \tag{2.18}$$

$$\mathbf{D} = \mathbf{d}\boldsymbol{\sigma} + \boldsymbol{\epsilon_\sigma}\mathbf{E} \tag{2.19}$$

instead of the stress charge form given in equations 1.1 and 1.2. Here $\boldsymbol{\varepsilon}$ is the strain vector, $\mathbf{s_E}$ is the compliance matrix measured under zero electric field, $\boldsymbol{\sigma}$ is the stress vector, $\mathbf{d}$ is the piezoelectric coupling coefficient matrix, $\mathbf{E}$ is the electric field vector, $\mathbf{D}$ is the electric displacement vector, and $\boldsymbol{\epsilon_\sigma}$ is the electric permittivity matrix measured under zero stress [18]. Equations 2.18 and 2.19 can be derived from equations 1.1 and 1.2 using

$$\mathbf{c_E} = \mathbf{s_E^{-1}} \tag{2.20}$$

$$\mathbf{e} = \mathbf{d} \cdot \mathbf{s_E^{-1}} \tag{2.21}$$

$$\boldsymbol{\epsilon_\varepsilon} = \boldsymbol{\epsilon_\sigma} - \mathbf{d} \cdot \mathbf{s_E^{-1}} \cdot \mathbf{d^t} \tag{2.22}$$

The analysis of a multilayer piezoelectric cantilever will make some additional assumptions but will not make the assumption of *small piezoelectric coupling* (SPC) as most authors have done in the past. The stress is assumed to be uniaxial ($\sigma_{11} \neq 0$ while $\sigma_{22} = \sigma_{33} = 0$), and the electric field is assumed to be negligible in the x and y directions ($E_3 \neq 0$ while $E_1 = E_2 = 0$). It is also assumed that the piezoelectric material under consideration has the symmetry properties of a dihexagonal polar crystal of class $6mm$. Due to the simplifications inherent in these assumptions, s will denote s_{11}, E will denote E_3, ϵ will denote ϵ_{33}.

The equilibrium equations for the multilayer beam can be integrated through the thickness to get equations for axial force and bending moment given [26]. If axial inertia and traction are neglected, the beam curvature can be expressed as

$$M = -w_{,xx}\overline{YI} - \overline{MV} \tag{2.23}$$

where

$$\overline{YI} = b\sum_{n=1}^{N} \frac{1}{s_n}\Big[\frac{1}{3}Z_{Ck} + \frac{1}{12}\frac{d_{31n}^2}{\epsilon_n s_n - d_{31n}^2}h_n^3\Big] \tag{2.24}$$

and

$$\overline{MV} = \frac{1}{2} b \sum_{n=1}^{N} \frac{1}{s_n} \frac{d_{31n} V_n}{h_n} Z_{Qk}. \tag{2.25}$$

In equations 2.23-2.25, a comma followed by a subscript denotes the derivative, the subscript k refers to the layer, s is compliance, d_{31} the piezoelectric coupling coefficient in the strain-charge form, ϵ is the electric permittivity, $V_n = \phi_n\Big|_{z=z_{k-1}} - \phi_n\Big|_{z=z_n}$ where ϕ is the electric potential, $Z_{Ck} = (z_n - zn)^3 - (z_{k-1} - zn)^3$, $Z_{Qk} = (z_n - zn)^2 - (z_{k-1} - zn)^2$, $h_n = z_n - z_{k-1}$, and zn is the neutral axis in the absence of piezoelectricity and is defined as

$$zn = \frac{1}{2} \frac{\sum_{n=1}^{N} \frac{1}{s_n} (z_n^2 - z_{k-1}^2)}{\sum_{n=1}^{N} \frac{h_n}{s_n}}. \tag{2.26}$$

With the expression for bending moment given in equation 2.23, the beam equation governing the bending motion of a slender beam can be written

$$-(w_{,xx} \overline{YI} + \overline{MV})_{,xx} + p_z = \rho A_c \ddot{w}_0. \tag{2.27}$$

Here, p_z is some uniform pressure in the z direction, A_c is the beam cross-sectional area, and ρ is the thickness averaged beam density. The beam has boundary conditions

$$w\Big|_{x=0} = 0 \tag{2.28}$$

$$w_{,x}\Big|_{x=0} = 0 \tag{2.29}$$

$$M\Big|_{x=L} = 0 \tag{2.30}$$

$$M_{,x}\Big|_{x=L} = 0. \tag{2.31}$$

In sensing applications, the voltage, V_n, in equation 2.25 is unknown while under voltage actuation, the voltage is a known inhomogeneous forcing term. Because of this difference, the case of applied voltage and voltage sensing will be handled

separately.

In the case of beam actuation, some voltage V_n is prescribed across each piezoelectric layer. If the applied force, p_z, is assumed to be zero and assuming harmonic excitation, the displacement profile for the beam is determined to be

$$\begin{aligned} w =& \frac{1}{2}\frac{\overline{MV}}{\overline{YI}\beta^2}\Big[\frac{\sinh(\beta L)-\sin(\beta L)}{1+\cos(\beta L)\cosh(\beta L)}(\sinh(\beta x)-\sin(\beta x)) \\ & -\frac{\cosh(\beta L)+\cos(\beta L)}{1+\cos(\beta L)\cosh(\beta L)}(\cosh(\beta x)-\cos(\beta x))\Big] \end{aligned} \tag{2.32}$$

where

$$\beta^4 = \frac{\rho\omega^2 b\sum_{n=1}^{N} h_n}{\overline{YI}} \tag{2.33}$$

and ω is the radian frequency. The short circuited resonant frequency of the beam (neglecting damping) occurs when $\cos(\beta L)\cosh(\beta L) = -1$ and the first resonance occurs when $\beta L = 1.875$. For cases where $\beta L << 1.875$, the actuation frequency is much less than the natural frequency of the beam and inertia can be neglected. In this case, the curvature is approximately constant with rexpect to x and given by

$$w_{,xx} = -\frac{\overline{MV}}{\overline{YI}}. \tag{2.34}$$

This equation for beam curvature can be used to determine the d_{31} coefficient of a cantilever of known geometry by applying a voltage and measuring the beam curvature. Previous authors have suggested extracting d_{31} by measuring the tip deflection. A more robust measurement would result from using multiple measurements along the length of the beam to determine beam curvature and extract the d_{31} coefficient from equation 2.34.

The assumption of SPC, when applied to a piezoelectric actuator, is the assumption that the electric field is constant in the thickness direction of the piezoelectric

material. This assumption is valid if and only if

$$\frac{1}{4}\sum_{n=1}^{N}\frac{d_{31n}^2}{\epsilon_n s_n - d_{31n}^2}\frac{h_n^3}{s_n} << \sum_{n=1}^{N}\frac{Z_{Ck}}{s_n}. \tag{2.35}$$

This condition is satisfied whenever $d_{31}^2/(\epsilon s) << 1$ for all materials in the laminate. This criterion is sometimes given as that necessary to assume SPC [24] but, as pointed out by others [28], the SPC assumption can be dependent upon the ratio of piezoelectric to structure thickness as well. When SPC can be assumed, $\overline{YI}$ given in equation 2.24 can be replaced with the simpler form

$$YI = \frac{b}{3}\sum_{n=1}^{N}\frac{1}{s_n}Z_{Ck}. \tag{2.36}$$

If the SPC assumption is valid and if only one piezoelectric layer is being actuated, the d_{31} coupling coefficient of layer k can be computed as

$$d_{31n} = -2\frac{h_n s_n YI}{Z_{Qk} V_n b} w_{,xx} \tag{2.37}$$

when a voltage V_n is prescribed across the layer and a curvature $w_{,xx}$ results. If SPC can be assumed, other piezoelectric layers can be either shorted or open-circuited.

In the sensing configuration, we consider some form of external mechanical or acoustical stimulation of the cantilever. When sensing voltage, it is assumed that the electrodes are connected to sensing circuitry with large input impedance such that electrons cannot flow from one side of the piezoelectric material to the other. The stress in the piezoelectric material, therefore, gives rise to an electric field.

Without assuming SPC, the deflection profile of a clamped-free multi-layer piezoelectric beam is

$$w = \frac{Pb}{2\overline{YI}\beta^4}(a_1\sin(\beta x) + a_2\cos(\beta x) + a_3\sinh(\beta x) + a_4\cosh(\beta x) - 2) \tag{2.38}$$

where

$$a_1 = \frac{\beta L[\sinh(\beta L)\cos(\beta L) + \sin(\beta L)\cosh(\beta L)] + 2\alpha \sinh(\beta L)\sin(\beta L)}{\beta L[1 + \cosh(\beta L)\cos(\beta L)] + \alpha[\cosh(\beta L)\sin(\beta L) + \cos(\beta L)\sinh(\beta L)]}, \quad (2.39)$$

$$a_2 = -\frac{\beta L[\sinh(\beta L)\sin(\beta L) - \cos(\beta L)\cosh(\beta L) - 1] + 2\alpha \sinh(\beta L)\cos(\beta L)}{\beta L[1 + \cosh(\beta L)\cos(\beta L)] + \alpha[\cosh(\beta L)\sin(\beta L) + \cos(\beta L)\sinh(\beta L)]}, \quad (2.40)$$

$$a_3 = -\frac{\beta L[\sinh(\beta L)\cos(\beta L) + \sin(\beta L)\cosh(\beta L)] + 2\alpha \sinh(\beta L)\sin(\beta L)}{\beta L[1 + \cosh(\beta L)\cos(\beta L)] + \alpha[\cosh(\beta L)\sin(\beta L) + \cos(\beta L)\sinh(\beta L)]}, \quad (2.41)$$

$$a_4 = \frac{\beta L[\sinh(\beta L)\sin(\beta L) + \cos(\beta L)\cosh(\beta L) + 1] + 2\alpha \cosh(\beta L)\sin(\beta L)}{\beta L[1 + \cosh(\beta L)\cos(\beta L)] + \alpha[\cosh(\beta L)\sin(\beta L) + \cos(\beta L)\sinh(\beta L)]}. \quad (2.42)$$

In equations 2.39-2.42,

$$\alpha = -\frac{1}{2}\frac{b\sum_{n=1}^{N} \frac{d_{31n}\Lambda_n}{s_n h_n} Z_{Qk}}{\overline{YI}}, \quad (2.43)$$

$$\Lambda_n = \frac{E_n}{2}\Big[\frac{Z_{Qk}\big(\sum_{i=1}^{N} \frac{h_i}{s_i} - \sum_{i\neq k} \frac{d_{31i}}{s_i} E_i h_i\big) - h_n \sum_{i\neq k} \frac{d_{31i}}{s_i} E_i Z_{Qi}}{\sum_{i=1}^{N} \big(\frac{h_i}{s_i} - \frac{d_{31i}}{s_i} E_i h_i\big)}\Big], \quad (2.44)$$

and $E_n = \frac{d_{31n}}{\epsilon_n s_n - d_{31n}^2}$. The voltage developed across layer k of this beam is

$$V_n = -\frac{1}{L}\Lambda_n \frac{Pb}{2\overline{YI}\beta^3}[a_1\cos(\beta L) - a_2\sin(\beta L) + a_3\cosh(\beta L) + a_4\sinh(\beta L)]. \quad (2.45)$$

In the case of free vibrations, the characteristic equation can be found by setting the denominator of equation 2.39 to zero giving

$$\cosh(\beta_n L)\cos(\beta_n L) + \frac{\alpha}{\beta_n L}[\cosh(\beta_n L)\sin(\beta_n L) + \cos(\beta_n L)\sinh(\beta_n L)] = -1. \quad (2.46)$$

This equation can be used to find the natural frequencies of the beam. If the beam is operating significantly below its first natural frequency, inertia can be neglected and the equations for displacement and output voltage simplify. The low-frequency displacement profile is

$$w = \frac{Pb}{\overline{YI}}\Big(\frac{1}{24}x^4 - \frac{1}{6}Lx^3 + \frac{3-2\alpha}{12(1-\alpha)}L^2x^2\Big) \quad (2.47)$$

and the voltage across a layer is

$$V_n = -\frac{PbL^2}{6\overline{YI}}\frac{1}{1-\alpha}\Lambda_n. \tag{2.48}$$

When SPC can be assumed, the sensing equations simplify considerably. The most robust method of determining the validity of the SPC assumption is to determine if $\alpha << 1$ and if equation 2.36 is true. Any time both of these equations are true, the SPC assumption is valid. The SPC assumption is also valid whenever $d_{31}^2/(\epsilon s) << 1$ for all materials. This check of SPC validity depends only on the piezoelectric material parameters. This shows that when using AlN, the SPC assumption is always valid but when using PZT (depending on the material parameters), the more extensive check might be necessary.

When SPC can be assumed, the beam deflection profile is equal to that of a non-piezoelectric multi-layer beam. The output voltage simplifies to

$$V_n = -\frac{PbL^2}{6YI}\lambda_n \tag{2.49}$$

where

$$\lambda_n = \frac{1}{2}\frac{d_{31n}}{\epsilon_n s_n}Z_{Qk}. \tag{2.50}$$

Table 2.1 summarizes the findings of this section.

2.2.2 Diaphragm Transducer Sensitivity

The use of a diaphragm instead of a cantilever can have advantages. If the SPC assumption can be made, as is the case for most piezoelectric materials used for MEMS, the sensitivity of a diaphragm transducer can be calculated by simply calculating the stress in the diaphragm piezoelectric layers and integrating over the electroded area. A low-frequency model of a circular tensioned plate subject to a uniform pressure load

	Without SPC	With SPC
Deflection Profile w^*	$\frac{Pb}{\overline{YI}}\left(\frac{1}{24}x^4 - \frac{1}{6}Lx^3 + \frac{3-2\alpha}{12(1-\alpha)}L^2x^2\right)$	$\frac{Pb}{YI}\left(\frac{1}{24}x^4 - \frac{1}{6}Lx^3 + \frac{1}{4}L^2x^2\right)$
Curvature $w_{,xx}{}^\dagger$	$-\frac{\overline{MV}}{\overline{YI}}$	$\frac{d_{31n}bV_nZ_{Qk}}{2h_ns_nYI}$
Natural Frequency $f^\ddagger$	$\frac{\beta_n^2}{2\pi}\sqrt{\frac{\overline{YI}}{\rho A_c}}$	$\frac{1.875^2}{2\pi L^2}\sqrt{\frac{YI}{\rho A_c}}$
Output Voltage $V_n{}^*$	$-\frac{PbL^2\Lambda_n}{6\overline{YI}}\frac{1}{1-\alpha}$	$-\frac{PbL^2d_{31n}Z_{Qk}}{12YI\epsilon_ns_n}$

* Assuming voltage sensing, low frequency
† Assuming voltage actuation, low frequency, one piezoelectric layer n
‡ Assuming voltage sensing

Table 2.1: Beam results with and without small piezoelectric coupling

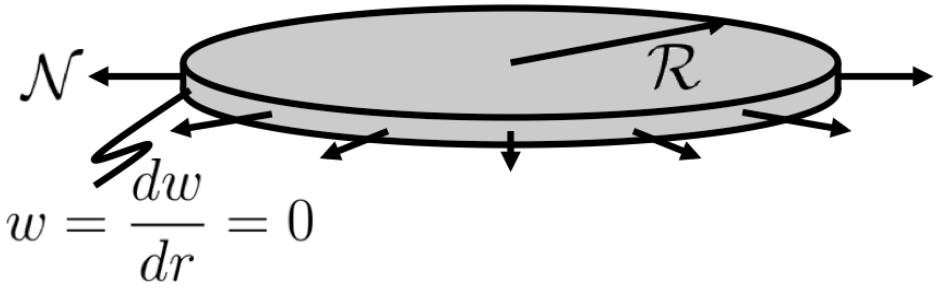

Figure 2.8: Tensioned Diaphragm with assumed boundary conditions.

will be presented. The dynamics will be ignored in the following model because it will be assumed that the A-weighted noise floor will be dominated by the low-frequency sensitivity of the device. Figure 2.8 shows a diagram of the diaphragm and assumed boundary conditions. A circular tensioned plate under a uniform pressure load is governed by the equation

$$\mathcal{D}\nabla^4 w - \mathcal{N}\nabla^2 w = P \tag{2.51}$$

for small displacements where w is the lateral displacement of the diaphragm, $\mathcal{R}$ is the diaphragm radius, P is the applied pressure, T is the diaphragm tension per unit area given as

$$T = \frac{\sum_{n=1}^{N} T_k h_k}{\sum_{n=1}^{N} h_k} \tag{2.52}$$

$\mathcal{N} = \mathrm{T} \cdot \sum_{n=1}^{N} h_k$, the diaphragm tension per unit length, and the flexural rigidity of the plate is

$$\mathcal{D} = \frac{1}{3} \sum_{n=1}^{N} \frac{Y_k}{1 - \nu_k^2} Z_{Ck} \tag{2.53}$$

where

$$Y_k = \frac{1}{s_{11k}} \tag{2.54}$$

and

$$\nu_k = -\frac{s_{12k}}{s_{11k}}. \tag{2.55}$$

Following the derivation of Timoshenko [51], the displacement is

$$w = \frac{P\mathcal{R}^4 \Big[I_0(\frac{\kappa r}{\mathcal{R}}) - I_0(\kappa) \Big]}{2\kappa^3 I_1(\kappa) \mathcal{D}} + \frac{P\mathcal{R}^2(\mathcal{R}^2 - r^2)}{4\kappa^2 \mathcal{D}} \tag{2.56}$$

where

$$\kappa = \mathcal{R} \sqrt{\frac{\mathcal{N}}{\mathcal{D}}} \tag{2.57}$$

and I is the modified Bessel function. In order to calculate the sensitivity, the stress must first be calculated. The stresses in the radial and azimuthal directions are

$$\sigma_r = \frac{Y}{(\nu + 1)(2\nu - 1)} [(\nu - 1)\epsilon_r - \nu \epsilon_\theta] \tag{2.58}$$

$$\sigma_\theta = \frac{Y}{(\nu + 1)(2\nu - 1)} [(\nu - 1)\epsilon_\theta - \nu \epsilon_r] \tag{2.59}$$

where

$$\varepsilon_r = \frac{d^2 w}{dr^2}(zn - zm), \tag{2.60}$$

$$\varepsilon_\theta = \frac{1}{r} \frac{dw}{dr}(zn - zm), \tag{2.61}$$

Y is the modulus of elasticity of the layer, ν is the poisson's ratio of the layer, zn is the distance to the neutral axis, and zm is the distance to the center of the piezoelectric layer. After the stress is calculated, the output voltage can be found using equation 2.19, and setting the average electric displacement over the electroded area to zero (assuming the output of the device has high impedance). This gives

$$V_{out} = \frac{d_{31} h_p}{A_e \epsilon_p} \int_{A_e} (\sigma_r + \sigma_\theta) dA_e \tag{2.62}$$

where A_e is the electroded area. After solving for stresses and plugging these values into equation 2.62, the output voltage is given as

$$V_{out} = \frac{1}{2} \frac{P d_{31} h_p (zn - zm)}{A_e \epsilon_p \kappa^2 \mathcal{D}} \frac{s_{11}}{(s_{11} - s_{12})(s_{11} + 2s_{12})} \int_{A_e} \frac{I_0(\frac{\kappa r}{\mathcal{R}}) - 2I_1(\kappa)}{I_1(\kappa)} dA_e. \tag{2.63}$$

The natural frequency of a tensioned circular plate can be found by solving

$$-\gamma_2 I_0(\gamma_1 \mathcal{R}) J_1(\gamma_2 \mathcal{R}) - \gamma_1 J_0(\gamma_2 \mathcal{R}) I_1(\gamma_1 \mathcal{R}) = 0 \tag{2.64}$$

where J and I are the Bessel function and modified Bessel function,

$$\gamma_1^2 = \frac{\mathcal{N} + \sqrt{\mathcal{N}^2 + 4\rho h \omega^2 \mathcal{D}}}{2\mathcal{D}} \tag{2.65}$$

and

$$\gamma_2^2 = \frac{-\mathcal{N} + \sqrt{\mathcal{N}^2 + 4\rho h \omega^2 \mathcal{D}}}{2\mathcal{D}} \text{ [52].} \tag{2.66}$$

In some cases, the diaphragm rigidity due to bending stiffness is much greater than that due to tension. If the value of the tension parameter, κ, is less than 2, then the tension in the plate can be ignored. This simplifies the expression for natural

frequency to

$$\omega_n = \left(\frac{3.196}{\mathcal{R}}\right)^2 \sqrt{\frac{\mathcal{D}}{\rho h}} \tag{2.67}$$

and that for displacement to

$$w = \frac{P}{64\mathcal{D}}(\mathcal{R}^2 - r^2) \text{ [51].} \tag{2.68}$$

The output voltage then becomes

$$V_{out} = \frac{1}{8}\frac{Pd_{31}h_p(zn - zm)}{A_e\epsilon_p\mathcal{D}}\frac{s_{11}}{(s_{11} - s_{12})(s_{11} + 2s_{12})}\int_{A_e} \mathcal{R}^2 - 2r^2 dA_e. \tag{2.69}$$

A uniformly pressurized diaphragm with clamped boundary conditions will have stresses of the opposite polarity on the inside (toward the center) versus the outside (toward the rim) of the diaphragm. If the electrodes covered the entire diaphragm uniformly, there would be no output voltage because the compressive stress would cancel with the tensile stress in equation 2.62. If the diaphragm has piezoelectric elements split where the stress transitions from positive to negative, the output voltage of either element would be

$$V_{out} = \pm\frac{Pd_{31}h_p(zn - zm)s_{11}\mathcal{R}^2}{64\epsilon_p\mathcal{D}(s_{11} - s_{12})(s_{11} + 2s_{12})}. \tag{2.70}$$

Note that in all equations, $2(zn - zm)h_p = Z_{Qk}$. This substitution makes the form of equation 2.70 appear similar to equation 2.49.

2.3 Linearity

Linearity is typically measured as a percent total harmonic distortion (THD) at a specific amplitude. THD is commonly calculated as either a ratio of harmonic to fundamental power or a ratio of harmonic to fundamental amplitude. The latter is

commonly used in audio so THD will be defined as

$$\text{THD} = \frac{\sum \text{harmonic amplitudes}}{\text{fundamental frequency amplitude}} \tag{2.71}$$

The piezoelectric element is expected to be extremely linear and so the THD will be dominated by the non-linearity of the common source amplifier. The total harmonic distortion of a common source amplifier with a JFET will be presented. To test the non-linearity of the microphone, high SPLs must be generated without generating harmonics of the fundamental frequency. This can be done by using a system of tubes designed to resonate at the frequency of interest but not at harmonics of this frequency. The design of this system will be presented as well.

2.3.1 THD of a Common Source Amplifier

To calculate the THD, a non-linear FET model must be used. This can be done by starting with the equation for a FET in the saturation region

$$I_D = \beta_0(V_{GS} - V_{TO})^2 \tag{2.72}$$

where β_o is the FET transconductance coefficient or Beta factor, V_{GS} is the gate-source voltage, V_{TO} is the FET threshold voltage, I_D is the total drain current, and channel length modulation has been ignored. Here, V_{GS} is a combination of the DC bias voltage and the signal giving $V_{GS} = V_B + v_{in}$. This gives the total drain current as

$$I_D = I_Q + 2\beta_0(V_B - V_{TO})v_i + \beta_0 v_i^2 \tag{2.73}$$

where I_Q is the quiescent current. The output voltage of a common source amplifier is this current multiplied by the load resistor

$$v_o = 2\beta_0(V_B - V_{TO})R_L v_i + R_L\beta_0 v_i^2 \tag{2.74}$$

where the quiescent current has been dropped because it is a constant. A sinusoidal input voltage of $v_i = V_0 \cos(\omega t)$ would result in an output of

$$v_o = 2\beta_0(V_B - V_{TO})R_L V_0 \cos(\omega t) + \frac{1}{2}R_L\beta_0 V_0^2 + \frac{1}{2}R_L\beta_0 V_0^2 \cos(2\omega t). \tag{2.75}$$

Because only the second harmonic exists in this model, the THD will be the amplitude of the second harmonic divided by that of the fundamental and is therefore

$$THD = \frac{V_0}{4(V_B - V_{TO})} \tag{2.76}$$

Since the 2sk3426 JFET has a threshold voltage of -0.312 V and the bias voltage will be held at 0 V due to the bias resistor between the gate and source, the overdrive will be 312 mV. This means that a THD of 3% will occur when the input voltage is at 26.5 mV and a THD of 10% will occur when the input voltage is at 88.2 mV.

2.3.2 THD Measurement Resonator

In order to measure the total harmonic distortion of the microphone, it is necessary to create a tone at a high SPL while keeping the harmonics of this tone quite low. Most loudspeakers have significant distortion at high SPLs so a system of resonant tubes has been designed. This system of tubes would ideally have a resonant frequency in the range of microphone sensitivity (preferably between 500 Hz-1 kHz) and nulls at harmonics of this frequency. These nulls will ensure that very little pressure reaches the microphones at harmonics of the resonant frequency of interest. A two-tube system has been devised to meet these requirements. A diagram of this system can be seen in Figure 2.9. In each tube, a right and left traveling plane wave is shown. The amplitudes of these plane waves will be determined by the boundary conditions. At $x = -L_1$, the volume velocity will be determined by that of the speaker. Pressure and volume velocity continuity apply at $x = 0$, and the velocity at $x = L_2$ is zero.

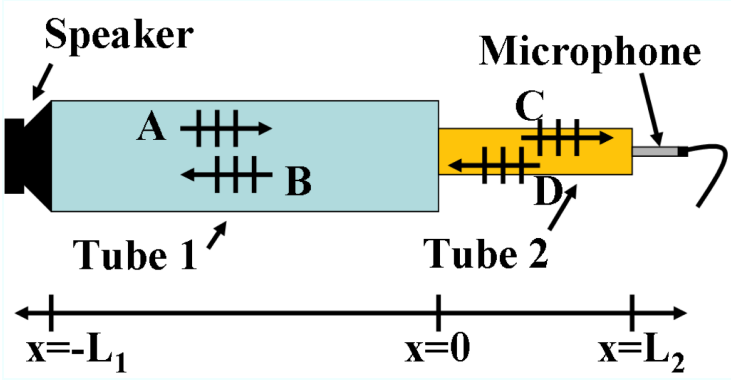

Figure 2.9: System of resonant tubes used to measure total harmonic distortion.

These four boundary conditions provide enough information to solve for the pressure at $x = L_2$ for a given speaker velocity. The frequency response of this system for $L_1 =$ 305 mm and $L_2 = 152.5$ mm can be seen in Figure 2.10. The first resonant frequency of this system occurs at roughly 500 Hz while the amplitudes at 1 kHz, 1.5 kHz, 2 kHz, 2.5 kHz, etc. are relatively low. This means that when the speaker in the front of the first tube is driven at 500 Hz, the harmonic levels are very low compared to this fundamental frequency. Therefore, any microphone output at harmonics of 500 Hz is due to microphone distortion.

2.4 Combining Piezoelectric Elements

As mentioned in the introduction, most piezoelectric microphones consist of at least two separate sensing elements due to the opposing stresses on the outside and inside of a deflected diaphragm. These two elements can be combined in series or parallel and, when done optimally, will conserve the output energy of the sensor. In other words, the square of the output voltage multiplied by the sensor capacitance will remain constant. A parallel combination of two identical elements will give twice the sensor capacitance of a single element and the same voltage. A series combination of two identical elements will give one half the capacitance of a single element but

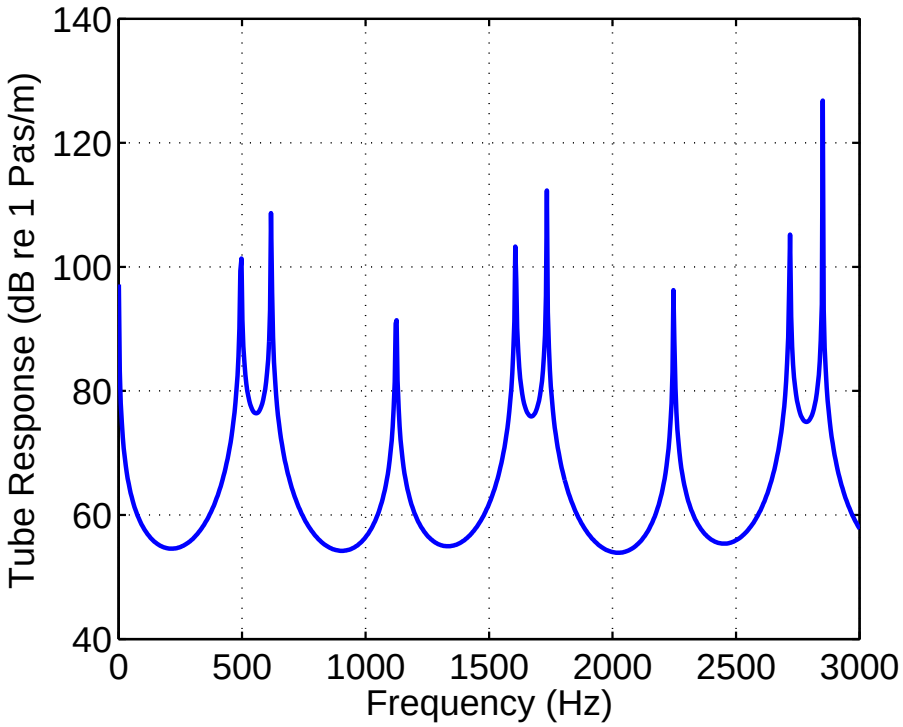

Figure 2.10: Modeled frequency response of two-tube system. Harmonics of 500 Hz are attenuated.

twice the output voltage. In both of these cases, the output energy is the same but the sensor capacitance is different.

Instead of limiting a design to two sensing elements, several elements can be used to provide a wide range of sensor capacitances but maintaining constant output energy. This idea can be used to determine the sensor capacitance which minimizes the input referred noise. For the example of a common source amplifier given above, an extremely large sensor capacitance can filter the thermal noise from R_b and the shot noise to the point that they are negligible and only channel noise dominates, however, this also reduces the output voltage coming from the sensor significantly. An extremely small sensor capacitance provides a large output voltage from the sensor but does not filter the thermal noise from R_b and can form a voltage divider between the sensor capacitance C_f, and the amplifier input capacitance C_{gs} so that the output voltage is attenuated significantly. The optimal capacitance value is one between these two extremes. For the example of the JFET used in a common source amplifier given above, the optimal sensor capacitance is 77 pF.

If the sensor capacitance is then fixed at this optimal value, the output noise of the circuit (ignoring the noise caused by the piezoelectric film resistance) will be fixed. If the output noise is fixed, the input referred noise is minimized by increasing the sensitivity of the sensor which is done by increasing the output energy of the sensor in response to an input. This shows that if piezoelectric film resistance is large enough to be ignored, a better sensor is one with greater output energy.

Now, it is important to determine how the piezoelectric film resistance affects the overall circuit noise. This can be done by comparing two sensing systems with two elements each, one wired in series and one in parallel as seen in Figure 2.11. Here, only the noise from the piezoelectric film resistance is being considered. Although each sensing element is identical, the two systems have different sensitivity, capacitance, resistance, and output referred noise as noted in Figure 2.11 using Laplace notation.

The input referred noise (v_{in}) however, is the same for both systems. This finding is true for any system of sensing elements regardless of the number of elements as long as they are combined in such a way as to preserve the output energy.

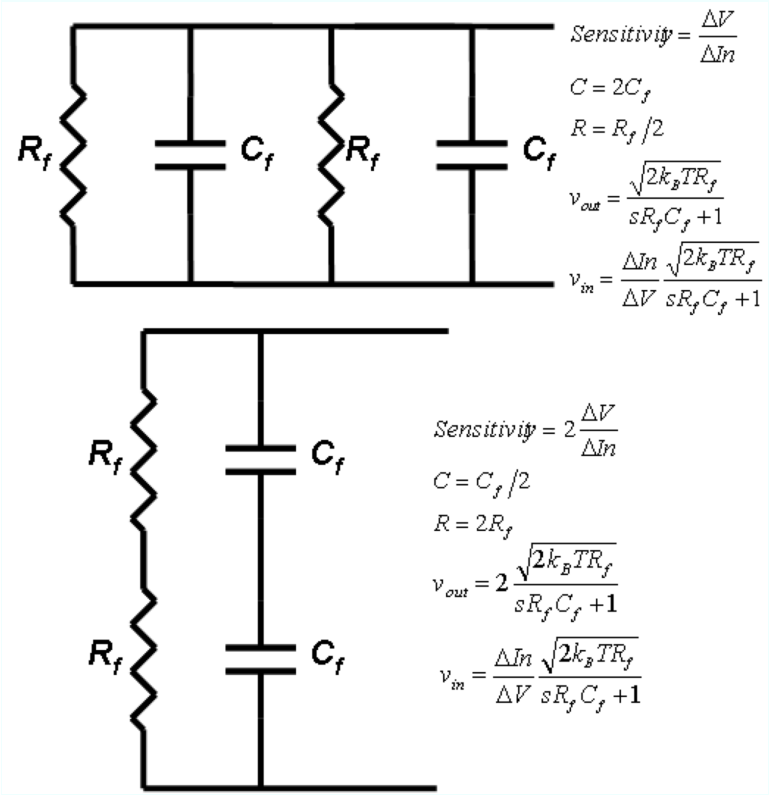

Figure 2.11: Effect of piezoelectric noise when sensing elements are combined in series and parallel.

2.5 Microphone Optimization

In the following section, piezoelectric microphones will be optimized using two different techniques. The first, simpler technique involves computing the output energy due to an applied acoustic pressure. While this technique is a simple way of comparing various beam shapes, electrode shapes, layer thicknesses and transducer geometries, it cannot be used to compare different materials and does not take into account electrode losses or material loss angle variations with material thickness. The

second optimization technique is similar to computing the total device signal to noise ratio and does include electrode losses and piezoelectric material loss angle. While the derivation of the optimization parameter is not as straight forward as output energy, it can be used to compare various materials, different transducer geometries, and can include all relationships between material properties and thickness.

2.5.1 Cantilever Transducer

2.5.1.1 Output Energy

The ideas presented in the noise section in combination with the sensitivity analysis shown above can be combined to design a piezoelectric cantilever microphone with a low noise level. For this design, it is reasonable to assume SPC because $d_{31}^2/(\epsilon s) << 1$ for both ZnO, AlN, and most forms of thin film PZT. Any errors caused by the SPC assumption can be checked after the design has been optimized.

If a cantilever beam is used and SPC is assumed, the output energy of one layer of a single beam can be computed. It is obvious that the addition of an identical beam will increase the output energy by two and so it makes sense to normalize the output energy to sensing area giving

$$\frac{V_{out}^2 C_f}{2p^2 bL} = \frac{b^2 L^4 d_{31n}^2 Z_{Qk}^2}{288(YI)^2 \epsilon_n s_n^2 h_n}. \tag{2.77}$$

Although this equation does not seem to provide much insight, a few important design aspects can be seen. First, since YI includes the width, b, the output energy per area is independent of beam width as would be expected with the given assumptions. Some of the parameters in equation 2.77 such as d_{31}, s_n, and ϵ_n, are material properties and are, therefore, fixed for a specific piezoelectric material. The design parameters are basically the length, L, and parameters that are related to layer thicknesses and relative layer compliances. This equation also shows that the output energy can be

increased by increasing the length of the beam but this, according to Table 2.1, will decrease the natural frequency, decreasing the bandwidth. Therefore, comparisons of output energy should be done while adjusting the length of the beam such that the natural frequency is constant.

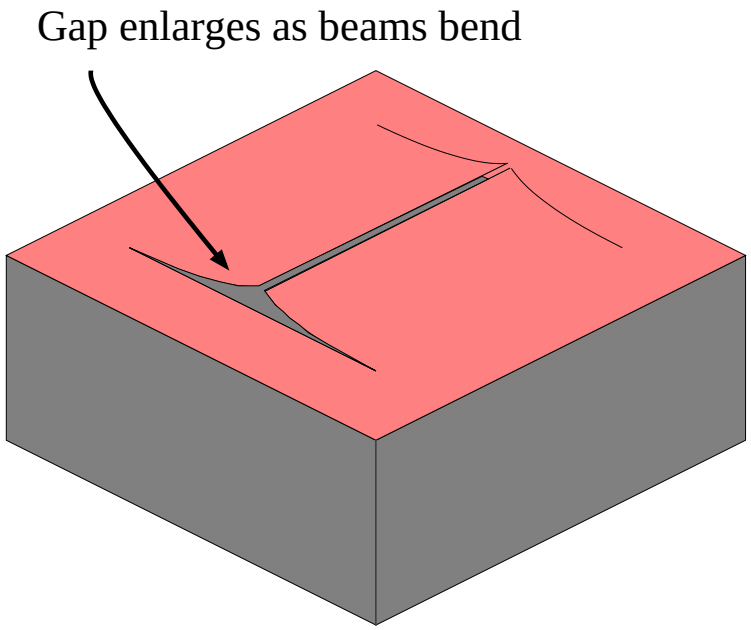

Figure 2.12: As the beams bend due to residual film stress, the gap around the beams increases, reducing the acoustic resistance of the microphone and decreasing sensitivity.

The general cantilever layer stack used for the optimization will be a five layer stack consisting of electrode/piezoelectric/electrode/piezoelectric/electrode layers. It is important to make the piezoelectric stack symmetrical when building a cantilever microphone because asymmetry in the stack can cause beam curvature. Beam curvature will increase the gap around the cantilevers, thus providing a path for pressure equalization and desensitizing the microphone as seen in Figure 2.12. Only the electrode material is used between the two piezoelectric layers because the piezoelectric material orientation depends upon the surface roughness and orientation [53]. The addition of a different material may cause the piezoelectric material quality to de-

grade and leave the top piezoelectric material useless. This would decrease the output energy per area by half.

With the cantilever layer stack determined, the output energy per area can be optimized by adjusting layer thicknesses and beam length while keeping the beam natural frequency constant. As a modeling example, a beam with Molybdenum (Mo) electrodes, AlN, and a natural frequency of 20 kHz has been analyzed. The Mo thickness has been adjusted from 1 nm to 1 μm and the AlN thickness has been adjusted from 500 nm to 2.3 μm. In this example, all three electrode layers were of equal thickness as were both piezoelectric layers. The results of output energy per area can be seen in Figure 2.13. Figure 2.13 shows that the output energy of a five

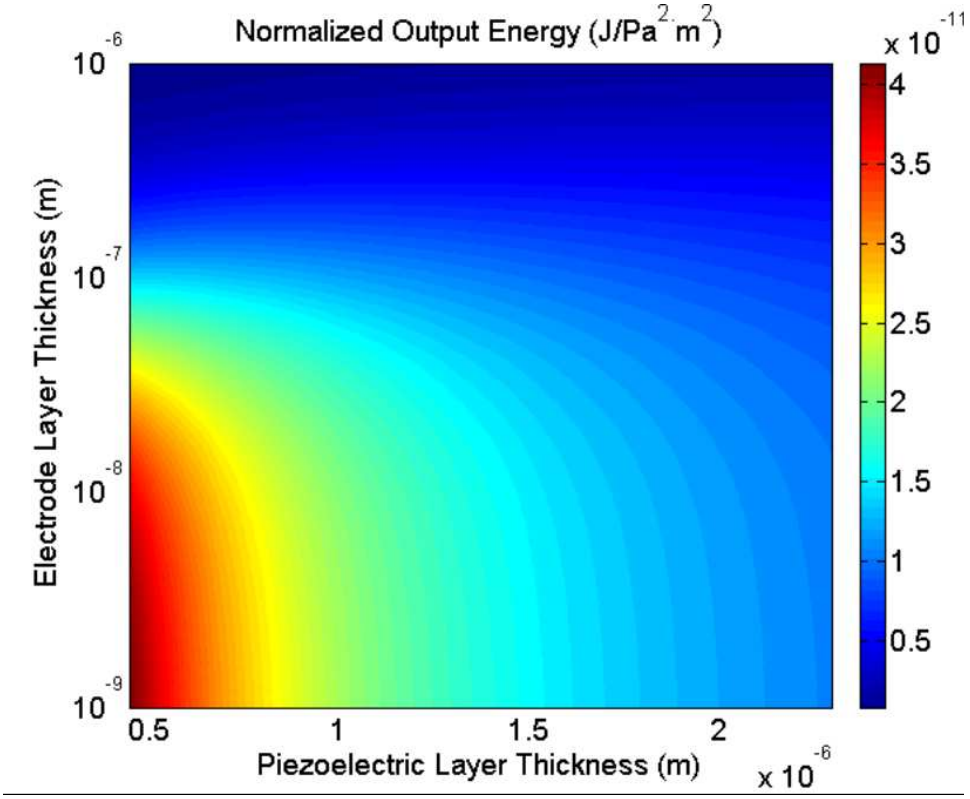

Figure 2.13: Theoretical output energy per unit sensor area. Thinner electrodes and thinner piezoelectric layers increase the output energy per sensor area.

layer cantilever beam under a uniform pressure load is increased as the piezoelectric layer thicknesses and electrode layer thicknesses are reduced. This reduction in layer

thickness, however, cannot go on infinitely. As the piezoelectric layer thickness is reduced, the average grain orientation is less consistent leading to reduced piezoelectric coupling coefficients. This reduction in piezoelectric coupling coefficient was not included in the calculation of normalized output energy. Additionally, the thinner layers have a much larger loss angle leading to additional noise in the sensor. The electrode layers, also, cannot be too thin. As the electrodes become thin, their resistance increases and they start to contribute to the overall noise as discussed in the noise section. Both thicknesses are also limited by manufacturability.

2.5.1.2 Optimization Parameter

To further investigate the limit to which these material thicknesses can be reduced, the total signal to noise ratio can be examined. For the same reasons given above, this signal-to-noise ratio will be normalized by the device area and natural frequency giving the following optimization parameter

$$\Psi = \frac{V_{out}^2 C}{P^2 A_s \tan(\delta)} f_{res}^2 \tag{2.78}$$

where V_{out} is the voltage out of the device, C is the capacitance of the device, f_{res} is the resonant frequency of the device, P is the applied pressure, A_s is the device area and $\tan(\delta)$ is the device loss angle. The only difference between this parameter and optimizing the normalized output energy is that it includes the loss angle. The square of the output voltage multiplied by the capacitance can be taken from equation 2.51. The resonant frequency can be taken from Table 2.1. The loss angle is given in equation 2.15. Putting these equations together, assuming the frequency in the loss angle calculation is equal to the resonant frequency and removing constants gives,

$$\Psi = \frac{1.875^4}{576\pi^2} \frac{b d_{31p}^2 Z_{Q_p}^2}{Y I \epsilon_p s_p^2 h_p \sum_{i=1}^{N} \rho_i h_i \left[\tan(\delta)_p + \frac{2*1.875^2 \epsilon_p}{3\sigma_e h_p h_e} \sqrt{\frac{YI}{b \sum_{i=1}^{N} \rho_i h_i}} \right]}. \tag{2.79}$$

While this model captures all the critical design variations, the material properties in the equation are constants while in reality, they will vary with material thickness. Most notably, both d_{31} and $\tan(\delta)$ tend to degrade as the film becomes extremely thin. These material property changes can be included by experimentally measuring their value as a function of material thickness, fitting a function to the data, and inserting this value in the optimization parameter calculation.

The Mo and AlN properties as a function of thickness are plotted in Figures 2.14(a)-2.14(c). Here, the AlN values have been taken from a study measuring AlN properties as a function of material thickness on platinum electrodes [54], and the Mo resistivity has been calculated using a model from the literature [49]. The values from these plots along with the other, less variable material properties can be used to calculate the optimization parameter as a function of layer thickness. When using the five layer device consisting of three Mo electrodes and two AlN layers used to generate Figure 2.15, the optimal sizing is seen in Figure 2.15.

Instead of the continual increase in performance with reduction in layer thickness shown in Figures 2.14(a)-2.14(c), Figure 2.15 shows that an optimal device will have 10 nm thick Mo electrodes and 1.5 μm thick AlN layers. These values, however, will vary because AlN loss angle and piezoelectric coefficients will depend on the tool used, the configuration of the tool, the electrode material used, surface roughness, and many other factors. For example, while the plot in Figure 2.14(b) shows that AlN of 0.5 μm thickness will have a loss angle of roughly 0.0034, the same author has deposited 0.5 μm thick AlN with a loss angle of 0.001 on Mo electrodes [55]. Additionally, manufacturing devices with 10 nm electrodes will be difficult without the use of advanced etch stop techniques or highly selective etches so thicker electrodes may be more practical.

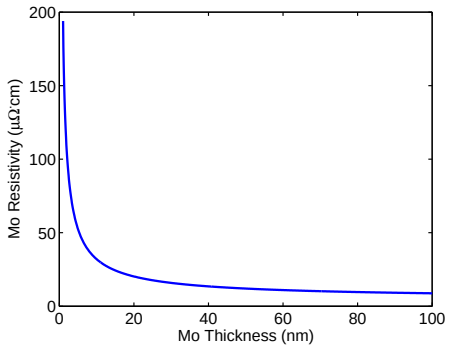

(a) Modeled Mo resistivity as a function of Mo film thickness.

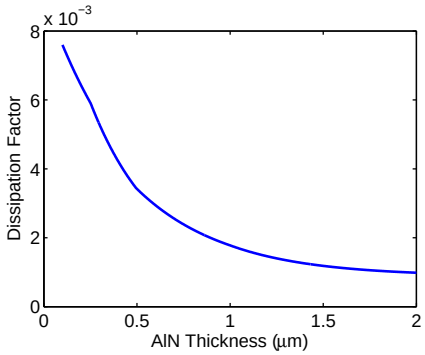

(b) AlN loss angle as a function of AlN film thickness extrapolated from measurements.

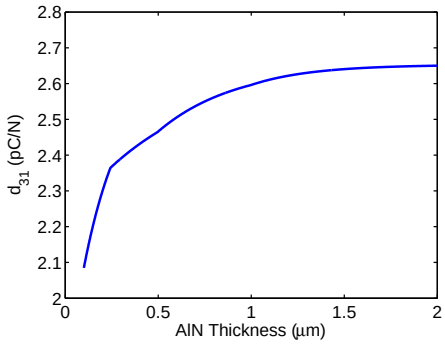

(c) AlN piezoelectric coupling coefficient as a function of AlN film thickness extrapolated from measurements.

Figure 2.14: Material properties of Mo and AlN as a function of layer thickness.

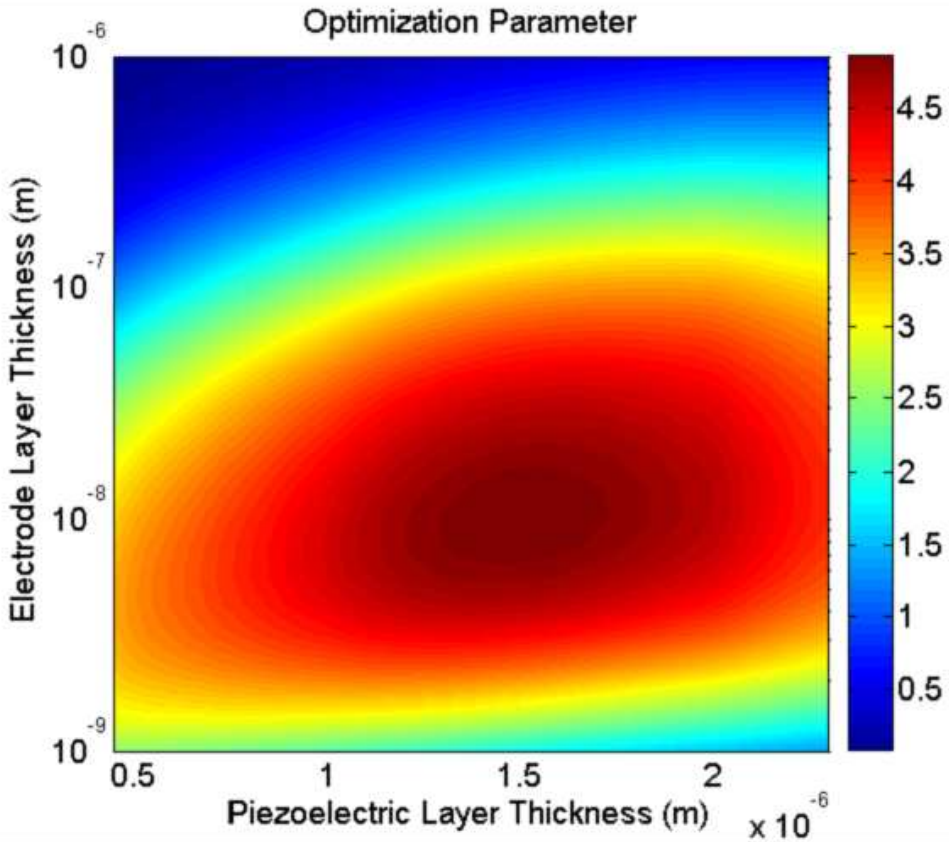

Figure 2.15: Optimization parameter, Ψ, as a function of electrode and piezoelectric layer thicknesses. The model gives optimal thicknesses around 1.5 μm AlN and 10 nm Mo.

2.5.1.3 Electrode Sizing

Not only can the output energy and optimization parameter presented in the previous sections be used to optimize layer thicknesses but they can also be used to optimize electrode coverage. Because changes in the electrode coverage cause only small variations in the noise power (shorter electrodes would have slightly less total loss), it makes sense to use the output energy to determine optimal electrode coverage for a cantilever microphone.

An applied acoustic pressure will induce the greatest amount of stress at the base of the cantilever, where the curvature is the largest. At the tip of the cantilever, the curvature, and therefore the stress, is small. If the electrode covers the beam

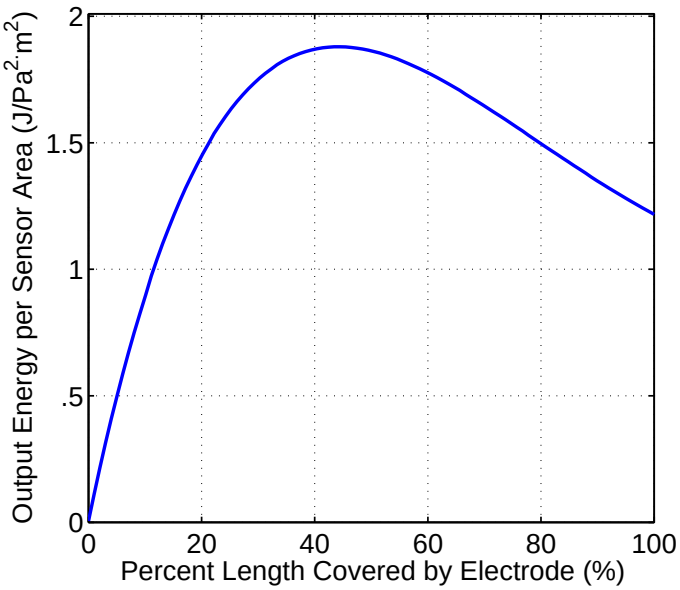

Figure 2.16: Theoretical effect of electrode length on normalized piezoelectric output energy. Decreasing the electrode length to around 45% increases the output energy by 54%.

from the base to the tip, the electroded area towards the tip of the beam acts as stray capacitance, reducing the sensitivity and therefore the output energy. If the electrode only coveres the first few microns towards the base of the beam, the output voltage would be very high as this is the area of greatest stress however, the output energy would suffer due to the small area and therefore low device capacitance.

Figure 2.16 illustrates this trade-off by adjusting the electrode coverage for a cantilever-based microphone with 1 μm thick AlN layers and 100 nm thick Mo electrodes. As shown in the Figure, if the electrode covers about 54% of the beam length, meaning that the electrode extends from the base of the beam to 54% down the length of the beam, then the output energy is maximized. By reducing the electrode coverage from the full length of the beam to the optimal value, the noise floor would be reduced by about 2 dBA. Similar results can be obtained for a diaphragm-based microphone.

	ZnO	PZT	AlN
d_{31} (C/N)	-5.74×10^{-12} [39]	-40×10^{-12} - -70×10^{-12} [36]	-2.65×10^{-12} [40]
d_{33} (C/N)	10.4×10^{-12} [39]	92×10^{-12}-203×10^{-12} [36]	5.53×10^{-12} [40]
s_{11} (Pa^{-1})	9.63×10^{-12} [39]	9.52×10^{-12}-14.9×10^{-12}[41]	3.53×10^{-12}[40]
$\tan(\delta)$	0.01-0.1 [36]	0.03-0.05 [42]	0.002 [42]
ϵ_{33}/ϵ_o	10.9[36]	1100-1300 [42]	10.4 [42]
ρ (kg/m^3)	5670	7600	3300

Table 2.2: Range of properties of common MEMS piezoelectric materials.

2.5.1.4 Piezoelectric Materials

Although output energy can be used to make several design decisions, it cannot be used to compare piezoelectric materials because it does not consider loss angle. If the noise of the amplifying circuitry is low, piezoelectric material with a large loss angle will be the dominant source of noise. Additionally, piezoelectric material properties depend on the electrode material upon which they are deposited so comparisons cannot be made by simply changing the piezoelectric material parameters. The optimization parameter is therefore necessary to determine which piezoelectric and electrode material combination is best. The material parameters taken from various sources in the literature can be seen in Table 1.1 which has been reproduced in this chapter for convenience.

Because ZnO and AlN have similar piezoelectric coupling coefficients but the loss angle of ZnO can be 100 times larger than that of AlN, this comparison will focus primarily on AlN and PZT. If PZT is used in place AlN and Platinum (Pt, commonly used as an electrode material for PZT) is used in place of Mo, the normalized output energy of a beam with two 1 μm thick PZT layers, three 100 nm thick Pt electrodes, and a resonant frequency of 20 kHz is 1.17×10^{-11} J/Pa^{2}m^2 when using properties in the middle of the ranges given in Table 2.2. This normalized output energy is slightly lower than that of a beam with equal thickness AlN and Mo layers with the same resonant frequency which has a normalized output energy of 1.25×10^{-11} J/Pa^{2}m^2

as can be seen in Figure 2.13. If comparing only output energy, one would assume that PZT would perform about the same as AlN but the lower loss angle of AlN gives it a much lower noise floor.

This lower loss angle is taken into account by using the optimization parameter for comparison. For the same Pt/PZT beam given above, the optimization parameter, $\Psi = 0.11$ m^2/kg while that for the AlN/Mo beam is $\Psi = 2.63$ m^2/kg. This analysis indicates that the beam utilizing AlN and Mo will be much better. When the model for sensitivity is combined with a circuit model of a JFET (2sk3426) in a common source amplifier circuit, assuming a sensor area of 1 mm^2 and a capacitance of 62 pF, the input referred noise is predicted to be 36.5 dBA for the AlN/Mo beam and 45.8 dBA for the PZT/Pt beam.

2.5.1.5 Other Considerations

Both Figures 2.13 and 2.15 show the motivation behind using MEMS technology. As the layer thicknesses are increased, keeping the ratio between layers the same, the output energy drops off significantly. This indicates that a high performance piezoelectric cantilever microphone cannot be built without the use of extremely thin material layers such as those possible with MEMS techniques.

The analyses used to create Figures 2.13 and 2.15 ignore stray capacitance. Stray capacitance will, undoubtedly exist in the traces on the chip, bond pads, and beam anchors but should be small for well designed systems. Fluid loading was, however, considered in the generation of these plots. The fluid loading is a function of sensor area and so, a sensor area of 1 mm^2 was assumed. Fluid loading can be included by adding some height of material with the density of air above and below the beam. This height can be approximated as $h_{air} = 8\sqrt{A_S}/3\pi$ where A_s is the sensor area [14, 46]. Fluid loading may be significant and will have a greater impact as beam thickness is decreased.

Despite not including stray capacitance, the noise floor can be estimated by calculating the output energy of the optimal device from Figure 2.15. Take, for example, a microphone that has a Mo thickness of 10 nm, an AlN thickness of 1.5 μm, generates output energy of 1.5×10^{-11} J/Pa^2 m^2 and has an area of 1 mm^2. The loss angle of AlN given in Table 1.1, in combination with the small signal model given in Figure 2.3 and an assumed sensor capacitance of 62 pF can be used to determine that this microphone would have a noise floor of 33 dBA. Judging from Figure 1.1, this noise floor would be extremely low for a piezoelectric microphone with 20 kHz resonant frequency.

2.5.2 Diaphragm Transducer

The use of a diaphragm instead of a cantilever is quite common for piezoelectric MEMS microphones [1, 44, 11, 12, 13]. For materials for which SPC is a valid assumption (criteria are slightly different for beam and diaphragm models), it is fairly simple to compare the output energy of a low stress diaphragm to that of a beam using equation 2.69. If the diaphragm is assumed to have low residual stress and act as a plate, thinner layers increase the output energy and, when optimized, the diaphragm provides more normalized output energy than a cantilever. However, when the layers become thin, residual stress becomes more likely to dominate the structural stiffness. For a Mo/AlN diaphragm with 100 nm electrodes and 1 μm AlN, the diaphragm residual stress must be less than 1.1 MPa to consider the diaphragm to be a plate [52]. The device normalized output energy is plotted against diaphragm stress for a five layer diaphragm with two 1 μm AlN piezoelectric layers and three 100 nm Mo electrodes in Figure 2.17. The diaphragm radius was adjusted to keep the natural frequency at 20 kHz. Residual stress below 1MPa is very difficult to achieve and is roughly equivalent to the resolution of common stress measurement tools [56]. As can be seen from Figure 2.17, increasing residual stress decreases the normalized output

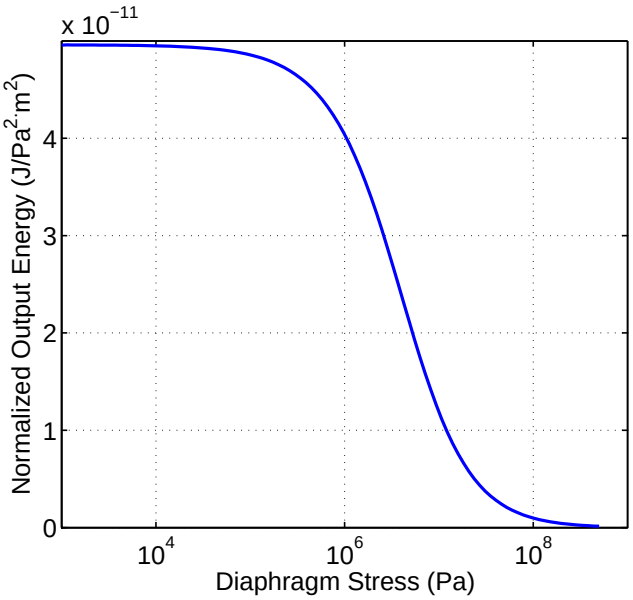

Figure 2.17: Models indicate that even small amounts of diaphragm stress significantly degrade the normalized output energy of a diaphragm of constant bandwidth

energy which will lead to an increased noise floor. Inconsistency in stress will also lead to inconsistency in sensitivity and bandwidth. For these reasons, any diaphragm based device must have low residual stress. If low residual stress cannot be achieved in the deposition tool, residual stress can be decreased after deposition by partially removing the diaphragm from the substrate and then reattaching it.

2.6 Packaging

The packaging requirements of a piezoelectric MEMS microphone are similar to those of capacitive MEMS microphones. The basic packages are shown in Figure 2.18. Both of these packages are similar to those used by commercial MEMS microphone manufacturers. The key aspects of these packages are an acoustic input, a back cavity volume behind the transducer, and a chip for buffering or amplification. There are many other methods of providing a package with these key aspects. These packages will be modeled along with the transducer to show the influence that packaging has

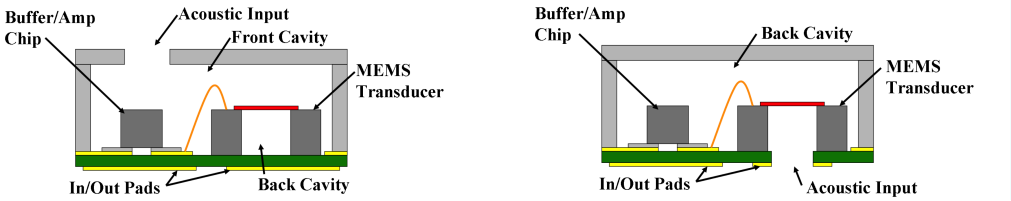

Figure 2.18: Two common embodiments of MEMS microphone packages.

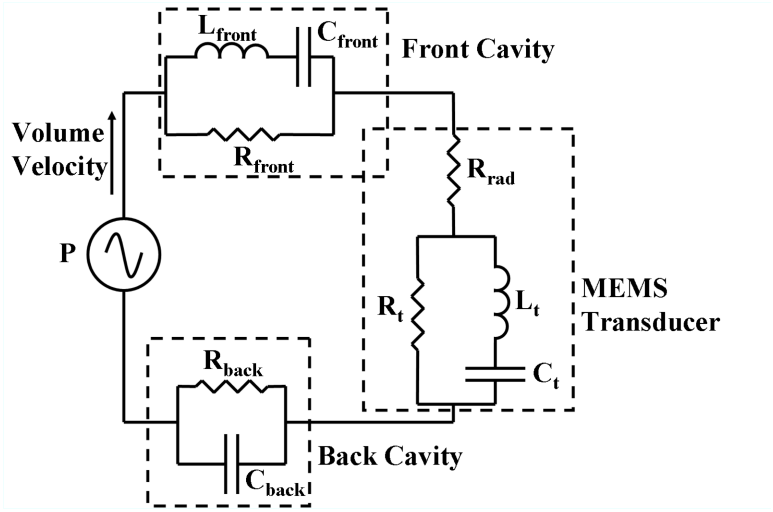

Figure 2.19: Package and device equivalent circuit. Includes any front cavity resonances, device response, and back cavity compliance.

on the overall microphone performance.

An equivalent circuit for the microphone and package can be seen in Figure 2.19. Because this is a lumped element model, only the first resonance of the microphone is included. In Figure 2.19, the front cavity may or may not be present depending on the packaging design. If using a design with a front cavity, the air mass moving in the acoustic input combines with the front cavity compliance to form a Helmholtz resonator [14]. The response of this Helmholtz resonator can be modeled using standard Helmholtz resonator equations [14] where lumped acoustic impedance parameters are

given as

$$L_{front} = \frac{\rho_0}{\pi \mathcal{R}^2}(L + 1.7\mathcal{R}) \tag{2.80}$$

$$C_{front} = \frac{\forall_{front}}{\rho_0 c^2} \tag{2.81}$$

$$R_{front} = \frac{\rho_0 c k^2}{4\pi} \tag{2.82}$$

In these equations, ρ_0 is the density of air, $\mathcal{R}$ is the radius of the acoustic input, L is the thickness of the acoustic input, V_{front} is the front cavity volume, c is the speed of sound (343 m/s in air at room temperature), and k is the wave number ($k = \omega/c$).

The cantilever or diaphragm will also have a dynamic response as modeled by R_t, C_t, and L_t. Because the transducer is now approximated as a second order system, the transducer model will only have a single resonant frequency. The acoustic impedance parameters for the transducer can be found as a function of diaphragm or cantilever displacement

$$C_t = \frac{\int_{A_s} w(x,y) dA_s}{P} \tag{2.83}$$

$$L_t = \frac{\int_{A_s} w(x,y)^2 dA_s}{\left(\int_{A_s} w(x,y) dA_s \right)^2} \tag{2.84}$$

Here, the mass loading can be included by adding an equivalent height of material with the density of air above and below the transducer. This equivalent height is

$$h_{air} = \frac{8\mathcal{R}}{3\pi} \tag{2.85}$$

for a circular diaphragm [14]. Similarly, the acoustic resistance of a small diaphragm in air at acoustic frequencies can be modeled as

$$R_r = \frac{1}{4\pi} \rho_0 c k^2 \tag{2.86}$$

The acoustic resistance to a volume of air traveling through the transducer will be determined by the size of hole in the diaphragm or gaps around the cantilever beams. Assuming the cantilever beams are flat, this acoustic resistance is given by

$$R_t = \frac{12\mu h}{g^3 l} \tag{2.87}$$

where μ is the coefficient of shear viscosity (1.85×10^{-5} Pa·s for air at room temperature), h is the total thickness of the cantilever, g is the width of the gap around the beams, and l is the total length of the gap, and $l >> g$.

Like the front cavity, the back cavity also has an acoustic compliance.

$$C_{back} = \frac{\forall_{back}}{\rho_0 c^2} \tag{2.88}$$

If the back cavity has some channel connecting it to atmospheric pressure, it will also have an acoustic resistance. If this channel is rectangular, the resistance will be

$$R_{back} = \frac{12\mu I}{h^3 w} \tag{2.89}$$

where l is the length of the channel, h is the height of the channel, w is the width of the channel, and $w >> h$.

Typically, it is desirable to make the packaging as transparent as possible. This means that, if the package has a front cavity acting as a Helmholtz resonator, the resonant frequency of the resonator is set above the frequencies of interest. Commercial capacitive microphones typically set this resonance around 15 kHz. In some cases, the back cavity compliance can be in the same range as that of the transducer. This is more common for cases in which the back cavity is formed by the back side of the MEMS chip. If the back cavity is not compliant enough, the equivalent circuit will, at intermediate frequencies, appear as a capacitive divider. This becomes a concern

as the transducer compliance becomes large, as is the case with the cantilever design. For example, a cantilever microphone with three 100 nm Mo electrodes and two 1 μm AlN piezoelectric layers requires a length of 384 μm to have a 20 kHz resonant frequency. A design consisting of two 384 μm long, 768 μm wide beams will have an acoustic compliance of 2.13×10^{-15} m^3/Pa. The back cavity compliance of a 768 μm $\times$ 768 μm $\times$ 500 μm volume is 2.07×10^{-15} m^3/Pa. This low back cavity compliance would reduce the signal by roughly 50%, therefore adding 6 dB to the noise floor and reducing the sensitivity by the same amount. It is therefore recommended that the cantilever design be used in a package where the back cavity volume is roughly that of the package. If the package is 3.75 $\times$ 4.75 $\times$ 1 mm and 50% is filled with air, the back cavity compliance would be 62.6×10^{-15} m^3/Pa. This compliance is roughly 30 times larger than that of the transducer and would have very little impact on the noise or sensitivity.

The diaphragm design is less compliant than the cantilever design making the above described performance degradation less severe. The same Mo/AlN stack given above would require a diaphragm with a 641 μm radius to achieve a 20 kHz resonant frequency (assuming the stress in the diaphragm is low). This diaphragm would have a compliance of 2.22×10^{-15} m^3/Pa. The back cavity, consisting of the volume behind the diaphragm, would have a compliance of 4.54×10^{-15} m^3/Pa if a 500 μm thick wafer was used and 5.90×10^{-15} m^3/Pa if a 650 μm thick wafer were used. Therefore, using a 650 μm thick wafer would result in only a 3 dB reduction in sensitivity and 3 dB increase in noise floor.

2.7 Vibration Sensitivity

An ideal microphone would be completely insensitive to vibration and sense only acoustic pressure. This, however, is not the case whenever a moving element with non-zero mass is used for transduction. The sensitivity to vibration, however, is fairly

simple to calculate. In order to calculate the sensitivity of a diaphragm or cantilever beam to vibration, it is only necessary to compute the acceleration that would result in the same force as an applied acoustic pressure. This acceleration depends only on the mass of the diaphragm or cantilever.

When modeling vibration sensitivity instead of pressure sensitivity, a uniform pressure load, P, can be replaced by an acceleration, a, using the equation

$$P_{equiv} = a \sum_{i=1}^{N} \rho_i h_i \tag{2.90}$$

where the device has i different layers of density, ρ, and height, h. This equation indicates that the vibration of a diaphragm or cantilever with a high mass per area would be sensed as a large pressure while one with a low mass per area would experience very little cross-sensitivity to vibration. The mass of the air above and below the diaphragm can be added into the summation for improved accuracy but typically contributes little to the overall sensitivity.

As an example of vibration sensitivity, a five layer microphone consisting of two 100 μm AlN layers and three 100 μm Mo electrodes with an area of 1 mm $\times$ 1 mm would have a vibration sensitivity of 0.011 Pa$\cdot$s^2/m or 0.11 Pa/g. This means that it would require an acceleration of 9.4 g to equal 1 Pa. When compared to other microphones, this vibration sensitivity is better than that of large capacitive microphones and electret microphones but slightly worse than capacitive MEMS microphones with lower mass diaphragms.

CHAPTER III

First Generation Device

3.1 Introduction

This section will cover the design, fabrication, and testing of the first generation piezoelectric MEMS microphone built for the present study. The design was based on the models developed in Chapter II. Many of the dimensions were relatively conservative due to fabrication uncertainties while others aspects of the design were overly optimistic. The fabrication was a four mask process which kept the fabrication relatively simple and quick but sacrificed some performance. The methods used to measure the piezoelectric material properties and microphone performance will be summarized here and used in Chapter IV as well. After measuring the piezoelectric material properties, the microphone performance measurements matched the performance anticipated by the model.

3.2 Design

The models and optimization in Chapter II indicate that high performance piezoelectric MEMS microphones are obtained for thin piezoelectric and electrode layers. Because high quality AlN has been deposited on Mo by others [57, 55], Mo was selected as the electrode material. Other materials such as Ti and Pt were investigated

but Ti did not work with the rest of the processing and Pt was denser than Mo, leading to reduced microphone performance. A Mo thickness of 200 nm was selected because the AlN etch had not been developed and the ability to etch through the AlN and stop before removing all Mo was crucial to device operation. An AlN thickness of 0.5 μm was selected because thinner AlN films led to better microphone performance and high quality AlN films at 0.5 μm had been demonstrated. The beam lengths were designed to provide microphone bandwidths spanning the audible range and the electrode length was equal to the beam length because the same mask was used to pattern both the AlN and Mo. In some cases, 24 beams extended over a large hole in the silicon while in other cases, only four wider beams covered the same area. Fewer beams is better because this creates fewer gaps leading to a larger acoustic resistance but it was feared that extremely wide beams may bend and twist due to film stresses.

3.3 Fabrication

Piezoelectric beams of lengths ranging from 200 μm to 450 μm and widths of 30 μm to 300 μm were constructed. These beams had a five layer stack of materials consisting of 0.2 μm Mo/0.5 μm AlN/0.2 μm Mo/0.5 μm AlN/0.2 μm Mo. The AlN layers were deposited in an AMS AlN sputtering tool at the University of California Berkeley facilities by Harmonic Devices. All other fabrication was performed in the University of Michigan Lurie Nanofabrication Facility (LNF).

The fabrication followed the steps shown in Figure 3.1. First, a 200 nm thermal oxide was grown on a bare Si wafer and 200 nm of Mo was sputtered and patterned using the first mask. All Mo layers were etched with a dilute mixture of Aqua Regia ($9\ H_2O : 3\ HCl : 1\ HNO_3$). Next, AlN and Mo were deposited and patterned with the second mask. All AlN layers were etched with hot (85° C) phosphoric acid. This AlN etch caused significant undercutting of the top Mo electrodes. These same AlN and Mo depositions were repeated and then patterned with the third mask. The fourth

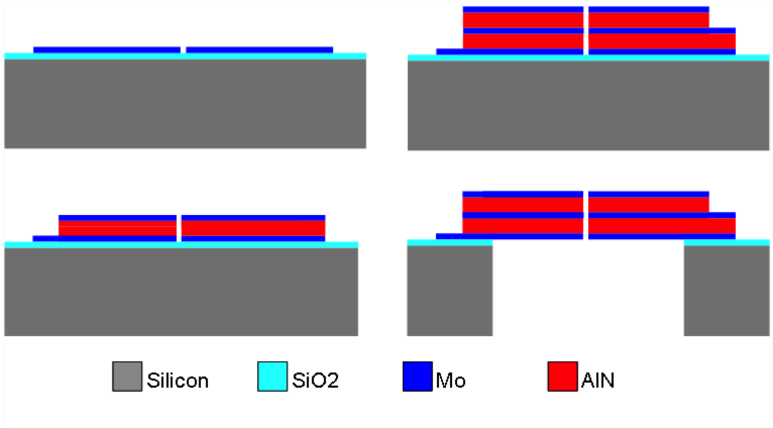

Figure 3.1: Four step beam fabrication process.

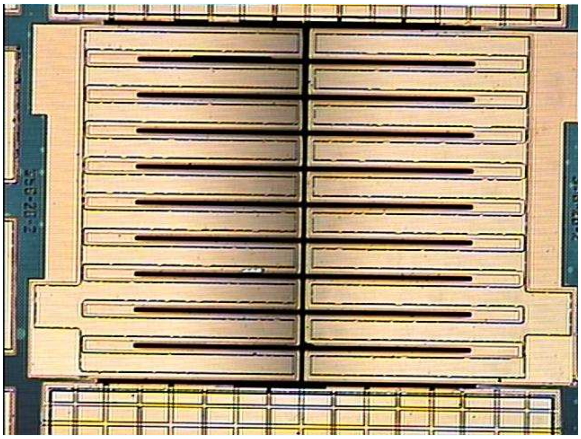

Figure 3.2: Microscope photograph showing the top view of twenty piezoelectric beams. These beams have five material layers on them and are released from the Si substrate.

mask was then used to pattern the back side hole which was etched through the wafer with deep reactive ion etching (DRIE). When completed, the beams appeared as seen in Figure 3.2.

When finished, the wafer was diced into 1.5 mm $\times$ 1.5 mm chips. Very few beams broke during processing. One drawback of this process is that the cross-wafer non-uniformity of DRIE means that the beam length varies from chip to chip. As the length varies, so does the sensitivity and bandwidth of the microphone. Another drawback of this process is that, because only four masks were used, the Mo cannot be patterned independently of the AlN. This increases stray capacitance and, if the

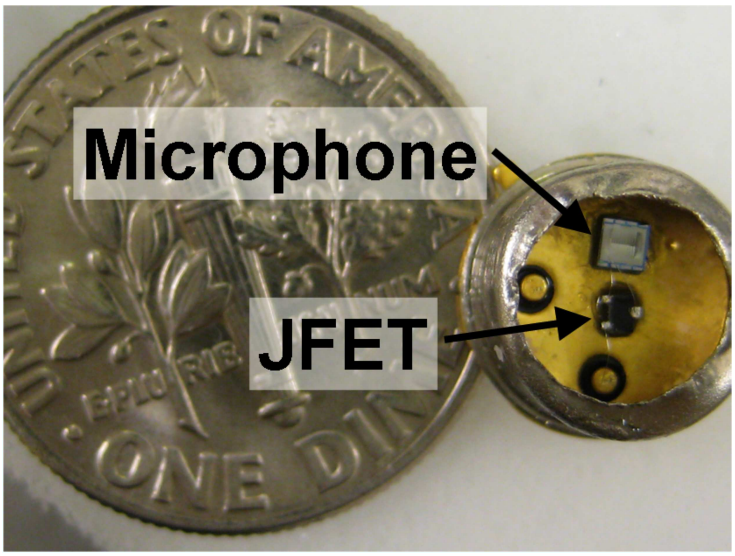

Figure 3.3: Packaged microphone wire bonded to JFET in TO can.

AlN etch undercuts too much, the two Mo layers can short together.

After dicing the wafer into chips, the chips were glued onto a transistor outline (TO) header with a hole drilled behind the chip. A JFET (2sk3426) was also glued onto the TO header and the chip was wire bonded to the JFET. Finally, a hole was drilled into a TO cap which was placed on the header. When completed, the microphone appeared as pictured in Figure 3.3.

3.4 Testing

After packaging, the microphones underwent a series of tests to determine material properties and microphone performance. First, the loss angle of the films was measured on both cantilevers and test capacitors using both an Agilent LCR meter and custom circuitry at 1 kHz. Unfortunately, the loss angle of the films tended to vary from about 0.01 to 0.1. It is believed that the loss angle of these films is significantly above that quoted in the literature for AlN because they are only 0.5 μm thick. Conversations with AlN tool manufacturers and with Harmonic Devices have indicated that X-ray diffraction rocking curves typically improve until the films

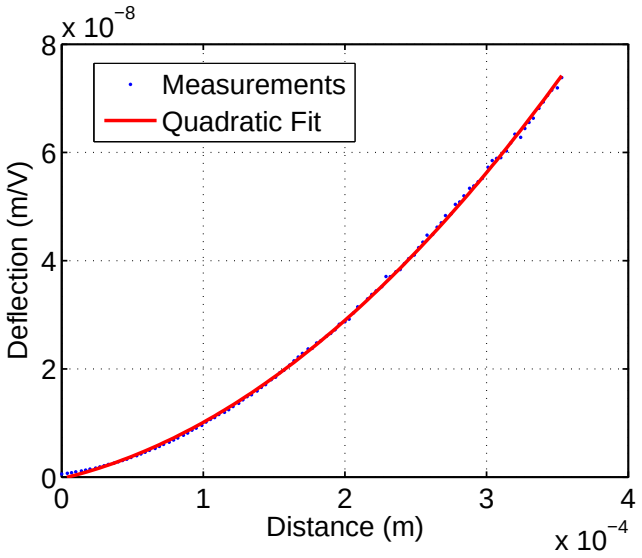

Figure 3.4: Beam actuation displacement measurements and quadratic fit used to calculate d_{31}.

reach 1-1.5 μm. Therefore, it is expected that these 0.5 μm films have degraded performance.

The d_{31} coefficient of the films was then measured by actuating the beams and measuring the beam deflection at several points along the length of the beam using a Polytec laser vibrometer as seen in Figure 3.4. These measurements were used to extract a resulting beam curvature and Equation 2.34 was used to calculate d_{31}. The d_{31} coefficient varied from -1 to -1.8 pC/N. This is slightly less than the d_{31} coefficient typically quoted in the literature and is consistent with what would be expected given the 0.5 μm films.

After measuring the d_{31} coefficient, the beams were exposed to a uniform pressure and the displacement and output voltage were measured. This was accomplished by using a plane wave tube as shown in Figure 3.5. A small speaker was placed at one end of the tube and the microphone and a calibrated Larson Davis 2520 reference microphone were placed equidistant from the speaker through holes in the side of the tube. Foam was placed in the end of the tube to provide an anechoic end condition. A Polytec laser vibrometer was focused on the back of the beams through the hole in

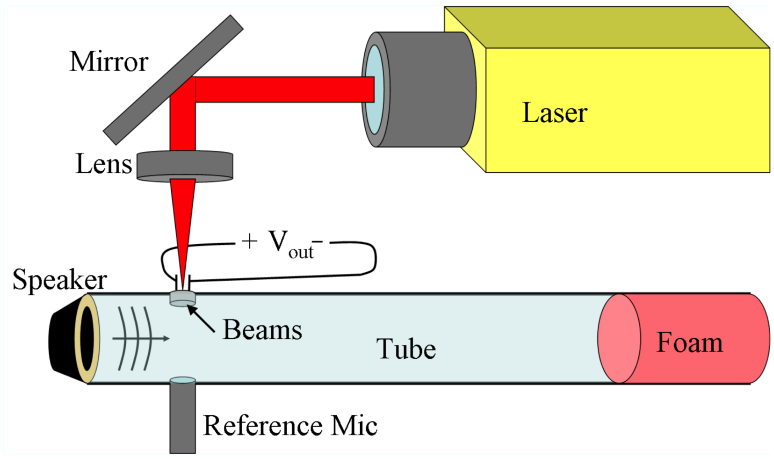

Figure 3.5: Test set-up used for measuring beam deflection and output voltage resulting from an applied acoustic pressure.

the TO header. This way, the beam displacement profile can be measured, as shown in Figure 3.6. A circuit with a 2.2 kΩ resistor and a 3 V supply was connected to the TO can to complete the common source amplifier. The output voltage of the microphone as a function of frequency was then measured as shown in Figure 3.7.

Figures 3.6 and 3.7 show that the beam displacement and microphone sensitivity match the models quite well when the measured d_{31} coefficient is used. The noise floor can then be measured by placing the microphone in a quiet, anechoic environment and measuring the signal out of the amplifier. The noise out of the amplifier, when connected to capacitors can be seen in Figure 3.8. The noise models given in Chapter II have been validated by placing low loss capacitors in place of the sensor and measuring noise. The piezoelectric noise dominates this sensor because the loss angle of the film is high.

3.5 Results

When the microphone measurements were completed, microphones with noise floors around 58 dBA were measured. Although these microphones were small, 2 × 10^{-7} m^2, the noise floor is only slightly better than average for piezoelectric micro-

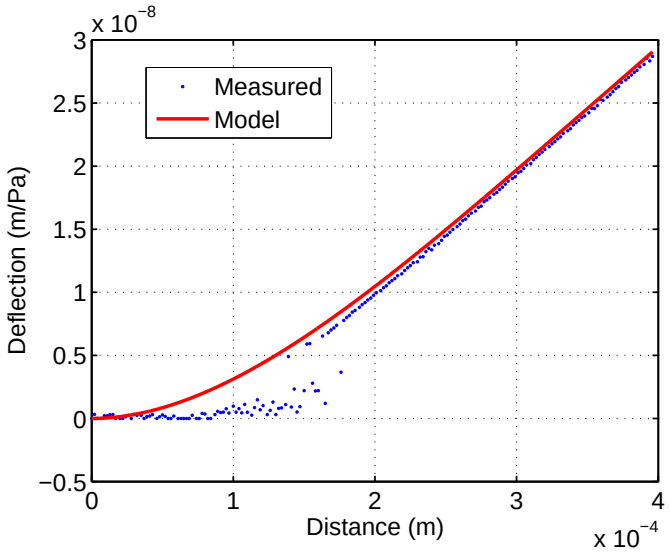

Figure 3.6: Beam deflection profile resulting from a uniform pressure load. The laser measurements towards the base of the beam were obstructed by TO can.

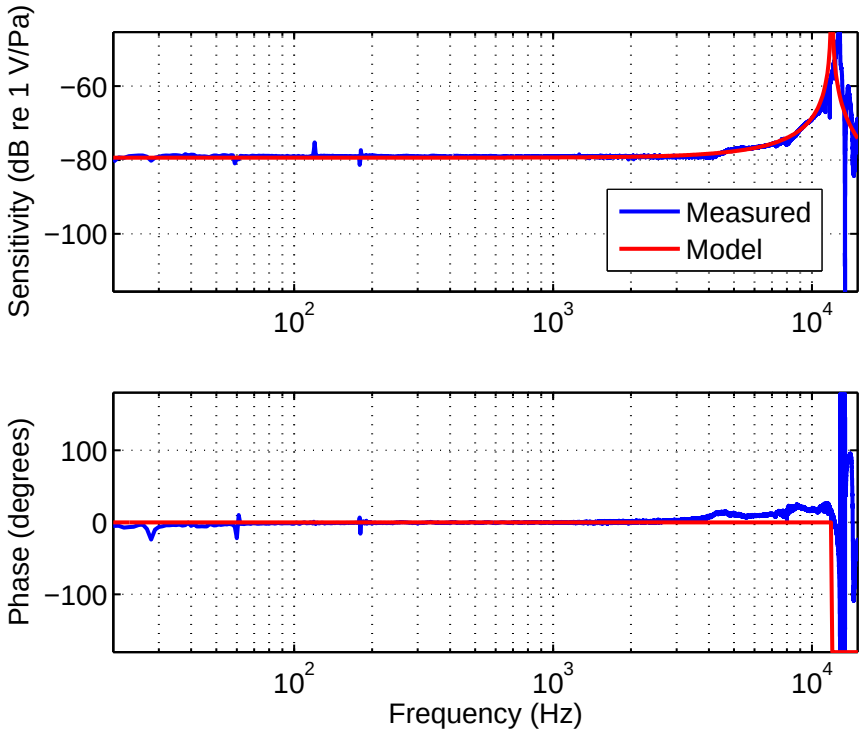

Figure 3.7: Amplitude and phase of the frequency response of the beams resulting from a uniform pressure load.

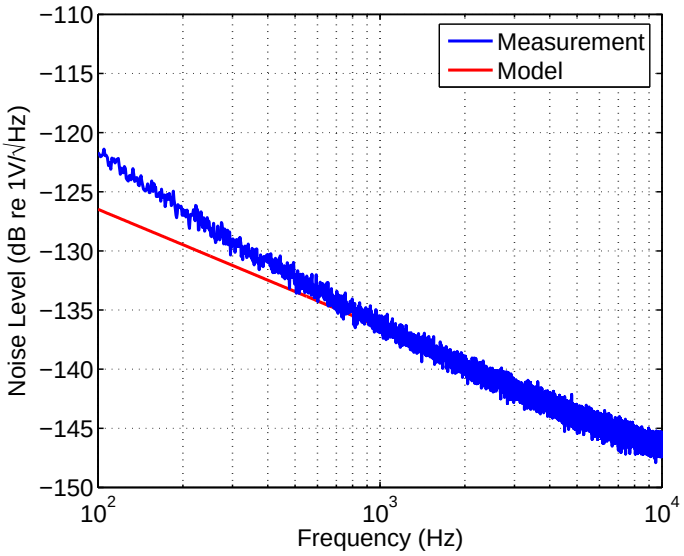

Figure 3.8: Measured and modeled output referred noise of common source amplifier.

phones of this size. This noise floor is somewhat limited by the piezoelectric coupling coefficient but mostly limited by the large loss angle. The inconsistency of films also prevented the use of both the top and bottom piezoelectric layers for sensing. The use of both layers will double the output energy and decrease the noise floor by roughly 3 dB.

The testing of this device provides validation that the sensitivity of the cantilever beam and the gain of the JFET were both modeled accurately. This testing also demonstrates, for the first time, that the piezoelectric noise of a piezoelectric MEMS microphone can be a dominant source of overall transducer noise. This first generation device also highlighted the difficulty of obtaining high quality AlN even when using a tool designed for AlN deposition. The etching of AlN also proved to be more difficult than anticipated. While the hot phosphoric acid etch provided a good way of etching AlN without etching Mo, the undercutting caused the Mo electrodes and leads between electrodes to be significantly undercut. This undercutting likely caused the electrodes to be shorted in some areas and may have been related to high loss angle measurements in others. Despite these difficulties, this first generation device proved

that several AlN based cantilevers could be fabricated with small enough deflection for use as a microphone. This device also showed that wide beams could be built without concern for beam curling or twisting. These lessons learned are applied to the second generation device discussed in Chapter IV.

CHAPTER IV

Second Generation Device

Many lessons were learned from the first AlN microphone design. First, it became clear that obtaining high quality AlN was not as simple as depositing the material with the right tool. It was hypothesized that the AlN loss angle was so high in the first design for three reasons. First, the AlN was only 0.5 μm thick and while some studies shown that high quality AlN can be deposited at 0.5 μm thickness [55], others show significant degredation of material properties at this thickness [54]. Second, the wet etching of AlN caused significant undercutting of the electrode material, often causing the electrode to crack or become discontinuous in narrow areas. As the electrode connections become narrow, the resistance increases, thereby increasing the loss angle. Third, it was thought that the AlN near the etched edge would be of poor quality and therefore have reduced performance. If this material was extremely lossy, it could increase the loss angle of the entire device.

The changes to the second design were primarily aimed at improving the loss angle. Two additional masks were added to the process so the Mo could be patterned separately from the AlN. This allowed the AlN to extend beyond the Mo electrodes so any AlN near an etch boundary would have a diminished impact on device performance. These additional mask layers also allowed for the electroded area to differ from the beam outline. By extending the electroded area over the first 50% of the beam length,

performance can be improved as shown in Figure 2.16 in Chapter II. The ability to pattern Mo separately from AlN also allowed for the design of a top interconnection layer to be used to connect various layers prior to wire bonding. Additionally, AlN thicknesses of 1.0 μm was deposited to increase the piezoelectric coupling coefficient and, more importantly, decrease the loss angle from the devices of the first generation. Improvements in material properties were also sought by improving the Mo properties. Studies have shown that the properties of the electrode material affect the AlN quality and models in Chapter II show that Mo of higher conductivity can improve the device loss angle. For these reasons, the Mo deposition parameters were adjusted to improve the Mo orientation and conductivity. Because the Mo of design two was of higher conductivity and because stopping the AlN etch on 200 nm of Mo was not a problem, the Mo thickness of design two was reduced to 100 nm.

The second microphone design also used two large flaps rather than several beams for the cantilevers. This change was made to reduce the total gap around the beams, increasing the acoustic resistance through the device. This change was aimed at reducing the necessary back cavity volume.

4.1 Fabrication

Using the design considerations of Chapter II along with lessons learned from the first device presented in Chapter III, cantilever microphones were built with Mo electrodes and AlN. These devices consisted of two wide piezoelectric beams with three, 100 nm Mo electrodes and two 1.0 μm AlN layers. As in design 1, the AMS AlN sputtering tool at the University of California Berkeley was used to deposit all AlN. This was again done by Harmonic Devices Inc. A 10-15 nm AlN seed layer was also used below the first Mo electrode because Tegal, the manufacturer of the AMS sputter tool used by Berkeley, had suggested it would improve Mo and AlN orientation. All processing other than the AlN deposition was performed at the

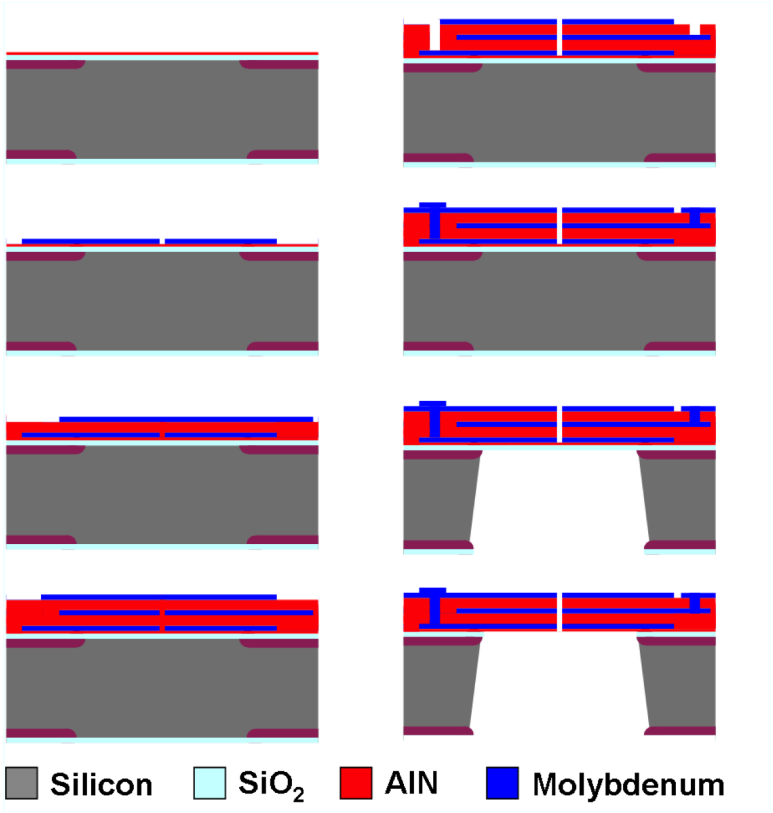

Figure 4.1: Piezoelectric MEMS microphone fabrication process. This is a 7 mask process without boron implantation and a 9 mask process with boron implantation.

University of Michigan LNF.

The fabrication followed the steps shown in Figure 4.1. In some cases, a deep boron implantation was used to pattern the front and back sides of the wafer. This boron implantation would later act as an etch stop, setting the beam length. The boron doping was used because cross-wafer variations in deep reactive ion etching (DRIE) led to variations in beam length in the previous generation of devices. Some devices did not use this implantation and, in these cases, a slower, high aspect ratio DRIE etch recipe was used to reduce the cross-wafer variation experienced in the first generation of devices. After boron implantation, 400 nm of thermal oxide was grown on the front and back sides of the wafer and the 10-15 nm AlN seed layer was deposited.

The first 100 nm Mo layer was sputter deposited at a pressure of 3 mTorr and 750 W power on the AlN. This layer was measured as 98 nm thick using a VEECO atomic force microscope (AFM) with an RMS resolution of 0.05 nm. This nominally 100 nm thick Mo layer had an average resistivity of 28 $\mu\Omega$cm measured by an FPP5000 four point probe and an average roughness of 0.592 nm RMS measured by an AFM. This Mo has a residual stress that varied from wafer to wafer but was approximately -700 MPa, where negative indicates compressive. Next, this Mo layer was patterned with dilute Aqua Regia (9:3:1 H_2O:HCl:HNO_3) using a photoresist mask. The first AlN layer was then deposited on the patterned Mo. This AlN layer had an x-ray diffraction (XRD) full width half maximum (FWHM) of 1.8° for 1.0 μm thick layers and 2.2° - 2.6° for 0.5 μm layers. The first AlN layer had a roughness of 2.01 nm RMS. The residual stresses in these layers were controlled by adjusting Ar and N_2 flow rates and the target stress was around 220 MPa for the 1.0 μm layer. The stress of the deposited material tended to vary due to inconsistencies in boron doping but was typically between 100 and 300 MPa.

After the first AlN deposition, the second Mo layer was deposited and patterned in an identical manner to the first. This second Mo layer had a slightly larger resistivity of roughly 35 $\mu\Omega$cm and a roughness of 2.02 nm RMS but the stress was almost zero. This low stress is significantly different than the extremely compressive stress of the first layer. The second AlN layer was then deposited in a manner identical to that of the first AlN layer. This AlN layer had an XRD FWHM of 2.0° for 1.0 μm thick layers and 2.3° to 2.6° for 0.5 μm thick layers. The top Mo layer was then deposited and patterned in the same manner as the first two and exhibited properties similar to the second. The AlN was then etched to form vias for metal interconnects and to form the beams. The first AlN etch went through only the top AlN layer and stopped on the middle Mo surface. This etch was performed in a LAM 9400 inductively coupled plasma etcher. The second AlN etch was performed in a similar manner but etched

through both AlN layers and stopped on the bottom electrode. In some cases, this etch was also used to form the beams while in other cases, a third AlN etch was used to form the beams. After all AlN etching, a top metal layer was deposited for metal interconnects. This layer was typically a 50 nm/500 nm Cr/Au layer. The Cr/Au was selected for its high conductivity.

Following the Cr/Au deposition, 12 μm of PECVD oxide was deposited on the top of the wafer and 3 μm PECVD oxide were deposited on the back side. The top oxide was deposited to protect the beams while dicing. The bottom oxide is then patterned and etched. This back side pattern aligns either the DRIE or TMAH etch to the front side of the wafer. If the wafer does not have boron doping, a DRIE pattern was always used. DRIE or TMAH were then used to etch from the back side of the wafer to the 400 nm thermal oxide layer on the front side of the wafer.

At this point, the beams are surrounded by oxide but free from the Si substrate. The wafer is then diced on a dicing saw. The dicing saw blade depth is slightly less than that of the wafer in order to prevent the saw from completely separating the chips. The wafer is then placed in a 7:1 buffered oxide etch (BOE) with surfactant to remove all oxide. The surfactant helps the BOE get to the bottom thermal oxide. The thin AlN seed layer is not specifically removed but is thin enough that it either breaks or is etched away in the BOE. After all oxide is removed, the chips are separated along the dicing lines and packaged. When finished, the devices appear as shown in Figure 4.2.

The packaging was also redesigned after the first iteration. The packaging consists of a $3.76mm \times 4.72mm$ patterned PCB, several of which are shown in Figure 4.3. The top side of the PCB is patterned for solder reflow of either a JFET, an amplifier similar to the National Semiconductor LMV1012, or allows the output of the MEMS transducer to be connected directly to the output pads. In some cases, a hole is drilled behind the MEMS transducer to allow the back cavity to be arbitrarily large

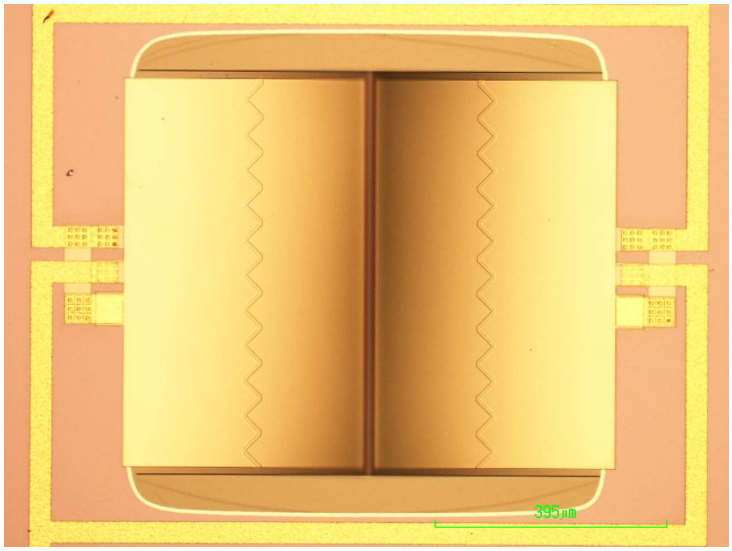

Figure 4.2: After fabrication is complete, the released beams appear as shown. The large compressive stress in the first electrode layer caused the beams to bend upward and are slightly out of focus.

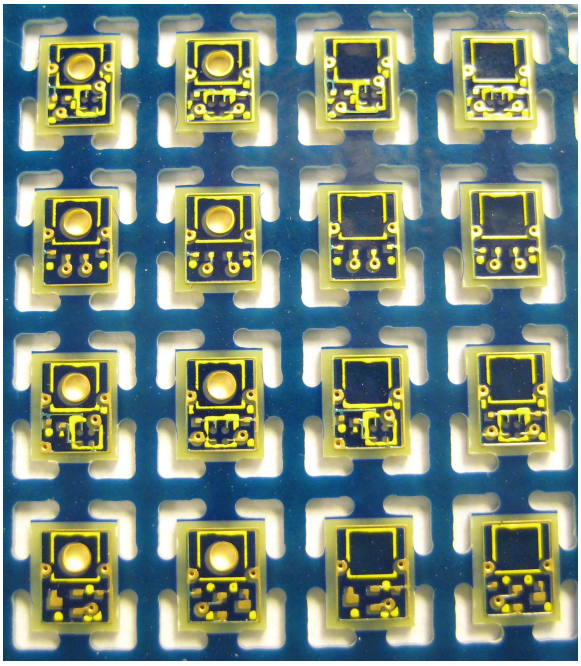

Figure 4.3: Several different PCB designs were fabricated for use with a variety of buffering techniques. Some designs have a hole behind the transducer in order to provide a larger back cavity volume.

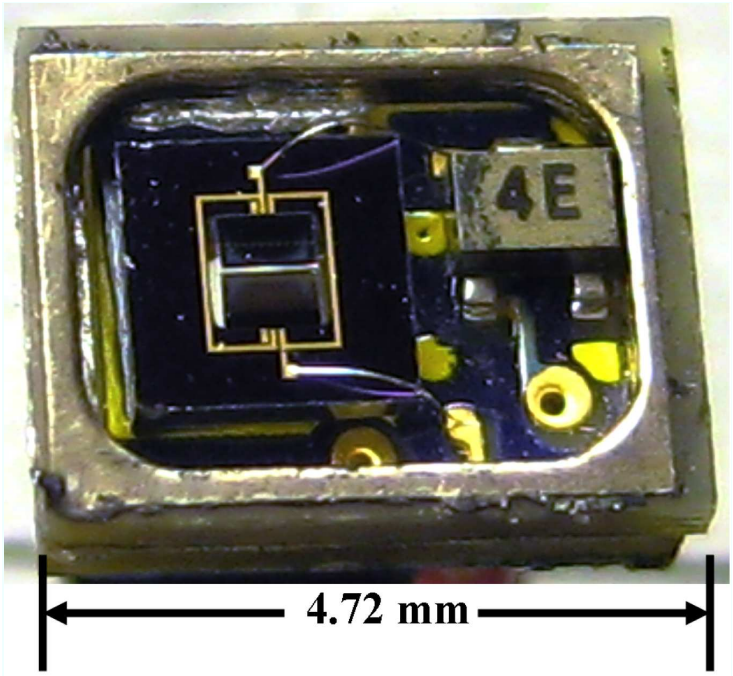

Figure 4.4: Packaged microphone transducer and JFET for signal buffering. There is no cap on this package to avoid any package resonance in the frequency response measurement.

or to allow the acoustic input to be placed behind the sensor. After separating a transducer chip from the wafer, the chip is glued to the PCB with Epo-tek T7139 electrically insulating epoxy. The chip is then wire bonded down to the PCB surface. Following wire bonding, the readout chip, usually a JFET, is attached to the PCB via solder reflow. After solder reflow, the microphone appears as shown in Figure 4.4. The back side of the PCB has pads for the signal output. In the case of the PCB with the JFET, there are pads for ground and output. The transducer and JFET are connected by wiring two 1.5 V batteries through a 2.2 kΩ resistor to the output pad and grounding the ground pad as shown in Figure 2.4. The output of the JFET can then go directly into a high impedance device for sound recording or can go through a preamplifier for additional signal buffering and electromagnetic interference rejection.

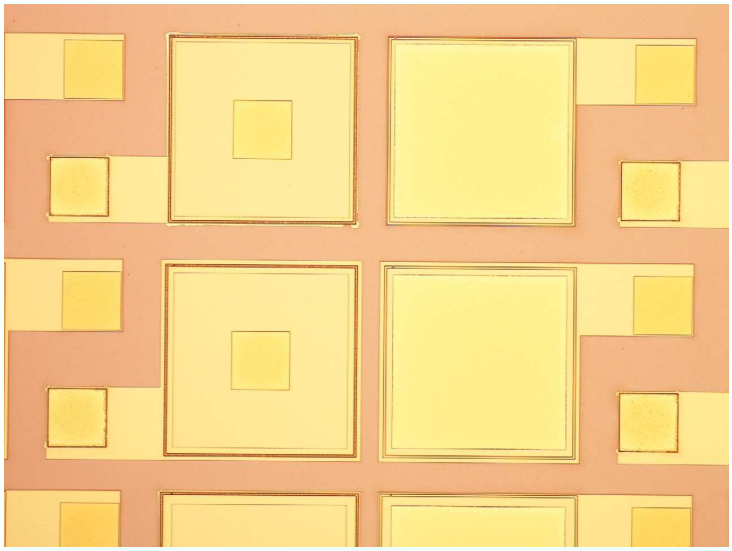

Figure 4.5: Four test capacitors. The capacitors on the left side of the figure are used to measure the bottom AlN film while those on the right side are used to measure the top AlN film

4.2 Testing

After packaging, the microphone and other test structures underwent tests to determine material properties and microphone performance parameters of interest. Most of the test procedures were covered in Chapter III, all other test procedures and results are detailed in this testing section.

4.2.1 Permittivity and Loss Angle

In order to test the hypothesis that low quality AlN near etch borders caused increases in loss angles, the loss angles of devices shown in Figure 4.5 were measured. These devices consisted of approximately 300 μm $\times$ 300 μm capacitors with AlN etches varying from 0 to 15 μm from the electrode edge. The figure shows two top (right side of the figure) and two bottom (left side of the figure) test capacitors with a square AlN etch 6 μm (top of the figure) and 10 μm (bottom of the figure) away from the capacitor edge. Four test capacitors of each type were measured at various points across the wafer and the results of these tests can be seen in Table 4.1.

AlN etch-Mo distance	Bottom C (pF)	Bottom tan(δ)(%)	Top C (pF)	Top tan(δ)(%)
$0\mu m$	8.04 ± 0.02	0.12 ± 0.04	7.67 ± 0.04	0.17 ± 0.05
$2\mu m$	8.07 ± 0.03	0.12 ± 0.04	7.68 ± 0.03	0.16 ± 0.05
$6\mu m$	8.06 ± 0.03	0.14 ± 0.04	7.69 ± 0.03	0.16 ± 0.05
$10\mu m$	8.07 ± 0.03	0.16 ± 0.04	7.69 ± 0.03	0.15 ± 0.05
$15\mu m$	8.06 ± 0.03	0.16 ± 0.04	7.67 ± 0.03	0.16 ± 0.06

Table 4.1: AlN capacitance measured for capacitors with different distances to etched AlN. The capacitance and loss angle was independent of the distance to etched AlN.

Bottom d_{31} (pm/V)	Top d_{31} (pm/V)
2.27 ± 0.2	2.48 ± 0.2

Table 4.2: Measured d_{31}. The top layer exhibited a slightly larger d_{31}.

These measurements were taken with an Agilent 4284A LCR meter using a shielded two terminal connection and a correction for the open circuit stray capacitance. This table indicates that neither the capacitance nor the loss angle varied significantly with the distance between the AlN etch and the Mo electrode. The top layer of AlN was 975 nm thick and the test capacitors were 295.5 μm $\times$ 295.5 μm. The bottom layer of AlN was 967 nm thick and the test capacitors were 297.3 μm $\times$ 297.3 μm. This gives an average relative dielectric constant of 9.7 for the top layer and 10.0 for the bottom layer. This relative dielectric constant is lower than that measured by most authors.

4.2.2 Piezoelectric Coupling Coefficient (d_{31})

After measuring the test capacitors to determine relative dielectric constant and loss angle, beams were actuated to determine the d_{31} piezoelectric coupling coefficient using equation 2.37. These measurements were performed on six different test cantilevers. On each test cantilever, both the top and bottom piezoelectric layers were measured separately. The results can be seen in Table 4.2.

This data indicates that the d_{31} piezoelectric coupling coefficient is slightly better in the top layer than in the bottom. Although the loss angles of the two layers would suggest that the they have approximately the same quality, other authors have shown that AlN with equivalent loss angles can have different piezoelectric coupling coefficients [54, 55].

4.2.3 Sensitivity and Noise Floor

With the given loss angles and piezoelectric coupling coefficients, the sensitivity and noise floor of the designed microphones can be predicted. The sensitivity can be estimated using equation 2.49. The noise floor can be estimated by modeling the output voltage noise of the common source amplifier, including the piezoelectric noise at the input of the common source amplifier, and then referring the noise back to the input using the sensitivity. Several different beam lengths were designed and fabricated. Here, a microphone consisting of two 395 μm long, 790 μm wide beams will be investigated. These beams have a 20 μm long, 790 μm wide anchor at the base, adding stray capacitance. These microphones are expected to have a low frequency sensitivity of 5.69e-4 V/Pa out of the piezoelectric transducer, 1.76e-3 V/Pa out of the common source amplifier, a natural frequency of 18.4 kHz, and an A-weighted noise floor of 35 dBA SPL. Several microphones of this size demonstrated similar performance with natural frequencies just above 18 kHz and sensitivity of roughly 1.8 mV/Pa at the output of the common source amplifier. One of these was selected at random for a more detailed performance characterization. All measurements were made in the same manner as those described in Chapter III.

The selected microphone had a sensitivity of 1.82e-3 V/Pa at 1 kHz out of the common source amplifier, and a natural frequency of 18.4 kHz. This microphone had an A-weighted noise floor of 37 dBA. A frequency response of this microphone can be seen in Figure 4.6. The plane wave tube used to measure the frequency

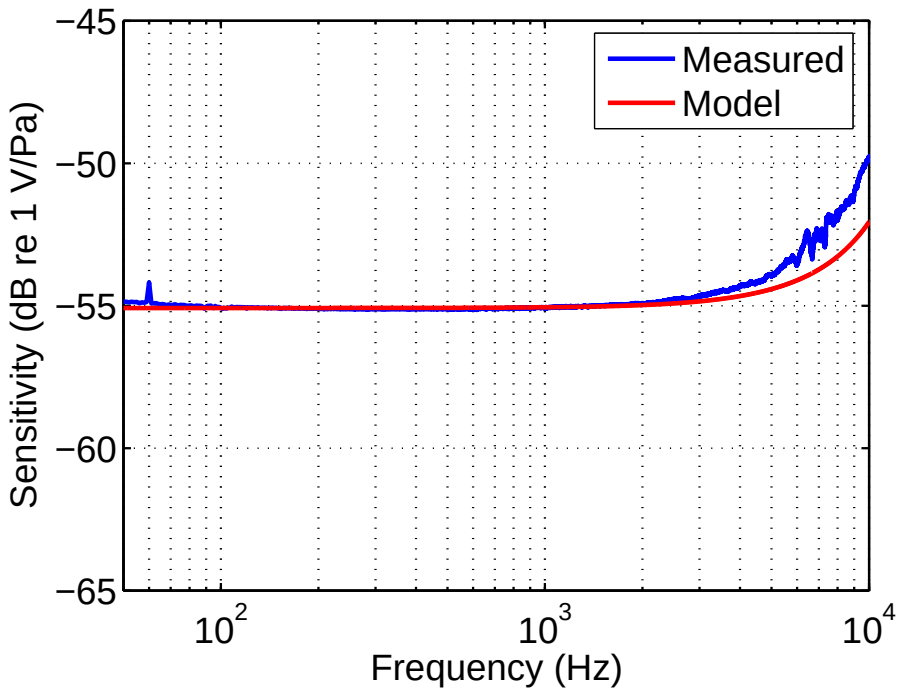

Figure 4.6: Sensitivity of a piezoelectric MEMS microphone with a 18.4 kHz resonant frequency. The increase in sensitivity at high frequencies is a characteristic of the plane wave tube.

response as described in Chapter III could not be used to measure the response of this microphone at frequencies as high as the microphone resonance. This is because at high frequencies, propagating modes other than the plane wave mode exist while at low frequencies, these higher modes are evanescent. This tube cut-off frequency is a function of its diameter.

The sensitivity of the microphone at 10 kHz increases beyond that of the model. This is caused by the plane wave tube and is not a true characteristic of the microphone. The noise floor measurement can be seen in Figure 4.7. The measured A-weighted noise floor (37 dBA) is roughly 2 dB higher than the modeled noise floor (35 dBA). Figure 4.7 shows that the difference between the modeled and measured noise floor occurred uniformly across all frequencies. The main cause for this discrepancy is most likely the material loss angle. A material loss angle of 0.3% would cause the observed increase in noise floor and increases the noise floor almost uni-

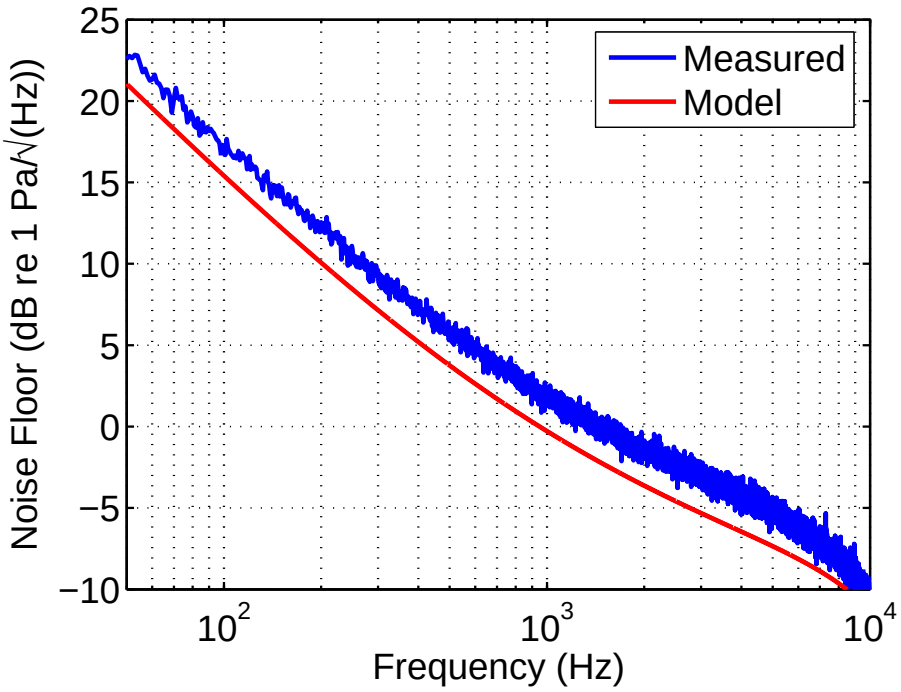

Figure 4.7: Noise floor of a piezoelectric MEMS microphone with a 18.4 kHz resonant frequency at room temperature. The modeled noise floor is roughly 2 dB lower than that measured but within the range expected due to the measured cross-wafer variation

formly through the frequency range shown above. Although this loss tangent would be higher than those measured, it would be less than two standard deviations away from the mean. Another cause could be a lower value of d_{31} in combination with a slightly higher common source amplifier gain. Although the sensitivity of the microphone matches the model quite well, the transconductance of the JFETs used in the common source amplifier can vary significantly from part-to-part. If the JFET transconductance was slightly higher than modeled and the d_{31} was slightly lower than modeled, the modeled sensitivity may still match the measurement but the input referred noise would be lower than expected. The 2 dB difference between measurement and model is likely a combination of these effects. A microphone with a 12.4 kHz resonant frequency was also measured and exhibited a 34 dBA noise floor.

These measurements were made with the back of the microphone open to the room. This makes the back cavity volume very large and so it has very little influence on the frequency response. The front cavity was also left off the microphone in order to avoid any package resonance. After releasing the beams, they became bent roughly 30 μm upward due to the large compressive stress of the bottom Mo layer. Because the beams were bent roughly 30 μm upward, the acoustic resistance, R_t, around the beams is lower than expected. This requires the back cavity volume to be large in order to have a low cut-off frequency set by R_t and C_{back} given in the packaging section of Chapter II.

4.2.4 Linearity

The linearity of the microphone was also measured. This measurement was made in the two tube resonator described in Section 2.3.2. The frequency response of this system was measured by applying a signal to the speaker and measuring the resulting output with a calibrated Larson Davis 2520 reference microphone. This system frequency response will, therefore, include the frequency response of the speaker as well

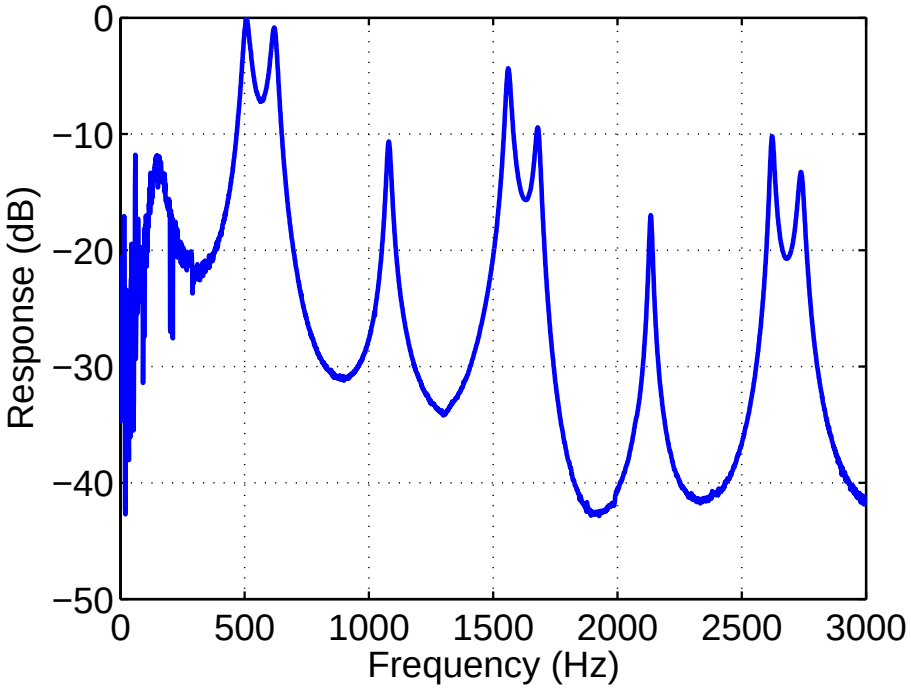

Figure 4.8: Measured frequency response of the resonant speaker/tube system.

as that of the tube system. The measured frequency response is shown in Figure 4.8. This response is similar to the modeled response of the system. When a tone is played at $500Hz$, the harmonics will be attenuated providing a low distortion pressure signal to the microphone.

After calibrating the microphone sensitivity, it was placed in the tube and the speaker was excited at 500 Hz. The total harmonic distortion of the signal was measured. The model predicts that this particular microphone amplified by a common source amplifier using a JFET (model 2sk3426) will have 3% THD at an output voltage of 82.0 mV RMS, 5% THD at 137 mV RMS, and 10% THD at 254 mV RMS. The measured output voltage at 3% THD was 85.5 mV RMS, at 5% THD was 149 mV RMS, and at 10% THD was 360 mV RMS. As the distortion increases, the measurements tend to stray further from the model but the predicted 3% THD level is quite accurate. In the other cases, the device outperforms the model. Using the calibrated sensitivity of this microphone, these distortion levels correspond to sound

pressure levels of 128 dB SPL at 3% THD, 133 dB SPL at 5% THD, and 140 dB SPL at 10% THD. With the use of more linear electronics, the distortion could be much lower at higher sound pressure levels.

4.3 Results

Microphones with two different resonant frequencies, 18.4 kHz and 12.4 kHz, were characterized and these microphones had noise floors of 37 dBA and 34 dBA. These measured devices did not have boron doping because the high aspect ratio DRIE etch recipe improved cross-wafer variation to an acceptable level. The boron doping tended to add roughness to the SiO_2 leading to a slight reduction in piezoelectric film quality. Unlike the first generation devices, these devices had a center electrode that spanned only about 50% of the beam which increased sensitivity and reduced the noise floor as expected. The properties of the 1 μm thick AlN were much better than those of the 0.5 μm micron thick AlN used in the first generation devices. This improvement is due primarily to the increase in thickness but also due to the use of an RIE etch instead of a wet etch used in the first generation devices. Unfortunately, the high stress in the bottom Mo layer led to a relatively large beam curvature which prevented these microphones from being placed in a package with a small volume. Future improvements should be made to reduce the necessary package volume.

CHAPTER V

Conclusions

Given the performance obtained in the previous chapter and that which is possible with further improvements, piezoelectric MEMS microphones show the potential for providing small microphones with much higher performance than that which is currently available commercially.

5.1 Demonstrated Performance

Figure 5.1 shows the noise floor of the microphones discussed in Chapter IV compared to other published works. These microphones have a noise floor 8 - 11 times lower than the best previously reported piezoelectric MEMS microphones using a sensing area only 62% - 92% that of previous devices.

Another way to compare microphones is to look at the output energy given as the $1/2 \cdot V_{out}^2 C_{mic}$ product or the $1/2 \cdot Q_{out}^2 / C_{mic}$ quotient at the output of these transducers caused by 1 Pa input pressure. With a sensitivity of 0.588 mV/Pa out of the piezoelectric transducer and a capacitance of 58 pf, the tested microphone with an 18.4 kHz resonant frequency develops a potential energy of 1.00e-17 Joules at the output. While the output signal prior to amplification of the capacitive microphone fabricated by Loeppert and Zinserling [29] is not given, it can be estimated through modeling. If the diaphragm has clamped boundary conditions, a 600 μm diameter

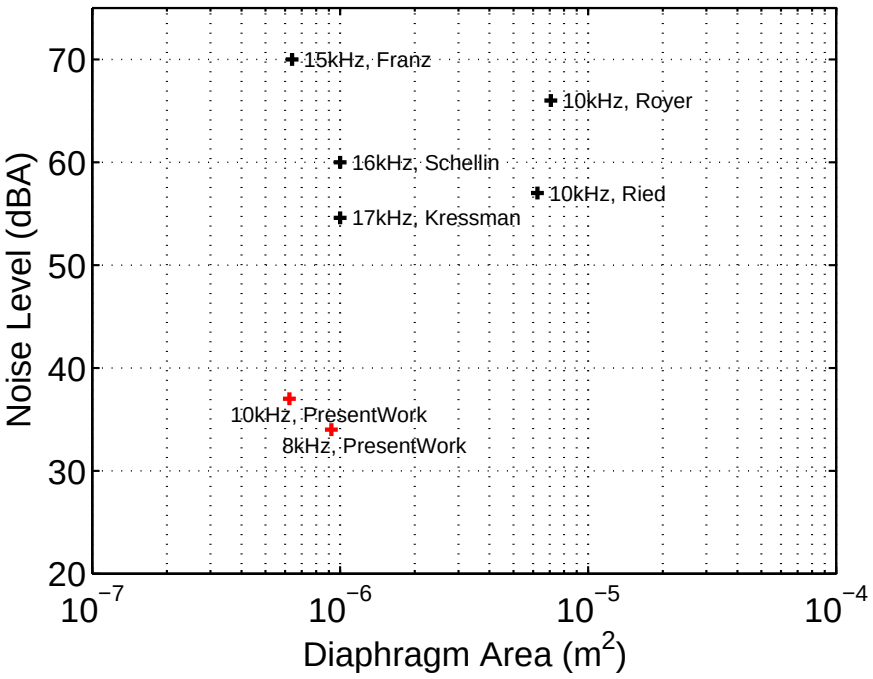

Figure 5.1: Piezoelectric MEMS microphone of present work compared to published works.

diaphragm would have a resonant frequency of 40 kHz and a center displacement of 2.7 nm/Pa. This displacement, in combination with an 11 V bias would result in an output energy of 3.13e-18 Joules. If the boundary conditions were not clamped but instead some combination of clamped and pinned, the output energy would increase and the resonant frequency would decrease. This means that if the tested 18.4 kHz resonance piezoelectric microphone had the same device capacitance as the capacitive MEMS microphone, it would be expected to have 1.8 times the sensitivity. Even if these devices had the same area, the piezoelectric MEMS microphone would be expected to have a greater sensitivity. Therefore, using the same circuitry, the input referred circuit noise would be lower for the piezoelectric MEMS microphone than this capacitive MEMS microphone. While the circuitry is not the only source of noise, this analysis shows that the circuitry used for these measurements does not have exceptionally low noise and further improvements to circuitry could be anticipated.

While the tested piezoelectric microphone discussed above has a greater output energy than the capacitive microphone, it also has a much lower resonant frequency. It would seem that a capacitive microphone with a lower natural frequency would have a greater output energy and a lower noise floor. While it is true that a more compliant diaphragm would result in a lower noise floor, it would also result in more distortion. A patent by Wang et al. illustrates this tradeoff [58]. This patent demonstrates capacitive MEMS microphones with a resonant frequency between 2 kHz and 3 kHz and a noise floor of 9.4 dBA but their models indicate that microphones like this will deflect 2/3 the gap height at a sound pressure level of 128 dB at which point the diaphragm will be pulled to the back plate. If a microphone stopped working when exposed to spikes in sound pressure levels exceeding 128 dB SPL, this would pose a problem as spikes in sound pressure levels above 128 dB SPL could be seen in a variety of situations. Of course, mechanical stops could be built into the microphone to prevent it from exceeding these levels but these would add fabrication complexity and more severe nonlinearity.

5.2 Further Performance Improvements

Although these microphones exhibit significantly improved performance over previously built piezoelectric MEMS microphones, there is still room for improvements. While the tested microphones used 100 nm thick electrodes and 1 μm thick AlN layers, the use of 25 nm thick electrodes and high quality, AlN at 0.6 μm thick would result in a 28 dBA noise floor for a device with a 15 kHz resonant frequency. A reduction in Mo thickness should be easily achievable with the use of an optical emission spectrometer to stop the AlN etch on the Mo electrode [59]. Further, the use of a low stress diaphragm should reduce the noise floor by an additional 4 dB over that of a cantilever based device of equal area. Additionally, the use of lower noise electronics could reduce the noise floor of these microphones by another 3 dB. All these

improvements will roughly add together resulting in extremely low noise microphones.

Over time, it is not unreasonable to expect that high quality AlN will be deposited at 0.5 μm thick because this has already been done in a laboratory environment [55]. It is also reasonable to expect that, by optimizing the circuitry for a piezoelectric MEMS microphone, the noise floor of the circuitry could be significantly below that of the piezoelectric material. If this is the case, a diaphragm with a 15 kHz natural frequency would have a radius of 509 μm and a capacitance (when sizing electrodes optimally) of 102 pf. This microphone would have a sensitivity of 1.45 mV/Pa and a noise floor of 20.5 dBA with noise free circuitry and a loss angle of 0.1%. If the natural frequency is increased to 40 kHz, the radius would be 312 μm, and the noise floor would be 33.2 dBA.

In addition to the potential for a lower noise floor, piezoelectric transduction offers greater linearity versus capacitive sensing. While the linearity of the fabricated devices has only been tested up to the limit of the common source amplifier, the use of a different amplification scheme should enable these microphones to sense extremely high sound pressure levels. The second generation devices resonate at 18.4 kHz, have an area of 6.27×10^{-7}, a noise floor of 37 dBA and experience 3% THD at 128 dB SPL. Although the linearity of these devices is limited by the amplification scheme, they are much more linear than any other microphone of similar size and noise floor. If a more linear amplification scheme was used, it is expected that these microphones would experience less than 3% THD at 165 dB SPL. If this is the case, these microphones would have a noise floor and dynamic range similar to 1/8" capacitive microphones which are roughly ten times the size of these piezoelectric microphones. For any application where dynamic range and size are the primary specifications of interest, well optimized piezoelectric microphones vastly outperform capacitive microphones.

5.3 Applications

The simplicity, linearity, small size, and low noise of the fabricated piezoelectric transducers make them ideal for a wide range of applications. The low noise, linearity, and simplicity make them ideal for aeroacoustic testing. Many aeroacoustic tests require the ability to sense loud sounds (165 dB SPL) without distortion. Most commercial capacitive microphones are used for consumer electronics devices and so most experience 3% THD between 105 dB SPL - 135 dB SPL. Some instrumentation quality capacitive microphones experience 3% THD between 160 dB SPL - 170 dB SPL but these are much more expensive than the microphones built for consumer electronics applications partly because they are larger and require more complex electronics. A piezoelectric MEMS microphone could offer a lower cost alternative to the capacitive microphones currently used for aeroacoustic tests.

The simplicity, small size, and low noise of these microphones make them ideal for consumer electronics applications. From the 1970s to the present, most microphones used in consumer electronics applications have been electret microphones utilizing an amplification scheme nearly identical to that used for these piezoelectric microphones. These electret microphones are very simple and relatively low noise. In 2003, commercial MEMS microphones were introduced. These microphones had slightly higher noise levels than many electret microphones but were smaller and could withstand higher temperatures, reducing the overall manufacturing cost. Piezoelectric MEMS microphones could offer the advantages of both microphone technologies by providing a low noise microphone with a simple amplification scheme while maintaining a small size and withstanding high temperatures.

5.4 Contributions

The contributions of this thesis are primarily aimed at reducing the noise floor of piezoelectric MEMS microphones. A complete electromechanical model of the microphone was used to investigate the limits of piezoelectric microphone technology. After developing the complete electromechanical model, it became clear that the MEMS transducer design and optimization could be separated from the circuit design. The ability to separate these two designs made design trade-offs and limitations more clear and understandable. Further, new models were developed to more accurately predict microphone performance and extract piezoelectric film properties from deposited films. Once the design trade-offs were fully understood, piezoelectric MEMS microphones were fabricated and tested. The models were experimentally validated. The contributions of this thesis have been summarized below.

- Developed a closed form solution for the sensitivity of a multi-layer cantilever beam without making the *small piezoelectric coupling* assumption
- Derived an expression used to determine the validity of the *small piezoelectric coupling* assumption or a multi-layer beam
- Developed and tested a method for measuring piezoelectric coupling coefficients using beam curvature
- Introduced the use of output energy as a metric for designing piezoelectric sensors, detailed the limitations of this metric, and provided design examples.
  - Used output energy to determine optimal electrode coverage for minimizing noise in a piezoelectric MEMS microphone
  - Used output energy to determine the influence of residual stress on the noise floor of a diaphragm-based piezoelectric MEMS microphone

  - Used output energy to compare cantilever-based piezoelectric microphones to diaphragm-based piezoelectric microphones

- Introduced an optimization parameter that can be used for designing piezoelectric sensors and provided design examples
  - Used the optimization parameter to determine the optimal layer thicknesses for minimizing noise in a piezoelectric MEMS microphone
  - Used the optimization parameter to compare piezoelectric materials for the fabrication of a piezoelectric MEMS microphone

- Built and tested piezoelectric MEMS microphones having a noise floor roughly ten times lower than the best previously published piezoelectric MEMS microphones.

5.5 Future Work

Future work should be focused on improving the microphone packaging and electronics. For some applications, the circuitry used during testing may be adequate but many applications will demand higher sensitivity, lower output impedance, better power supply rejection ratio, or lower power consumption. The use of an ASIC would improve all these metrics and could also reduce the noise floor. Because this is not a capacitive sensor, a bias is not necessary so the ASIC can be slightly simpler than those used for capacitive MEMS microphones.

The packaging also needs to be improved. For simplicity, packaging similar to that used for common commercial MEMS microphones was used for testing but a large back cavity volume was necessary because the beams were bent upwards. The beams need bend less than 2.5 μm at the tip in order to package the microphones in a reasonably small back cavity. To do this, AlN and Mo stress must be well matched

from one layer to the next. The ability to control residual stress of both of these materials has been demonstrated but a low deposition to deposition variation of this stress is crucial to ensuring flat beams. If beams with low tip deflection cannot be repeatably fabricated, a design with less sensitivity to stress must be examined. If this is the case, the fabrication of a stress relieved diaphragm or clamped-clamped beam will be necessary.

BIBLIOGRAPHY

BIBLIOGRAPHY

[1] M. Royer, J. O. Holmen, M. A. Wurm, and O. S. Aadland. Zno on si integrated acoustic sensor. *Sensors Acuators*, 4:357–362, 1983.

[2] D. Hohm and G. Hess. A subminiature condenser microphone with silicon nitride membrane and silicon back plate. *Journal of the Acoustical Society of America*, 85:467–480, 1989.

[3] J. B. Johnson. Thermal agitation of electricity in conductors. *Physical Review*, 32:97–109, July 1928.

[4] H. Nyquist. Thermal agitation of electric charge in conductors. *Physical Review*, 32:110–113, 1928.

[5] T. H. Lee. *The Design of CMOS Radio-Frequency Integrated Circuits*. Cambridge University Press, 1998.

[6] H. B. Callen and T. Welton. Irreversibility and generalized noise. *Physical Review*, 83:34–40, July 1951.

[7] V. Tarnow. The lower limit of detectable sound pressures. *Journal of the Acoustical Society of America*, 82:379–381, 1987.

[8] T. B. Gabrielson. Mechanical-thermal noise in micromachined acoustic and vibration sensors. *IEEE Transactions on Electron Devices*, 40(5):903–909, MAY 1993.

[9] P. R. Scheeper, B. Nordstrand, J. O. Gullov, B. Liu, T. Clausen, L. Midjord, and T. Storgaard-Larsen. A new measurement microphone based on mems technology. *Journal of Microelectromechanical Systems*, 12(6):880–891, DEC 2003.

[10] R. P. Ried, E. S. Kim, D. M. Hong, and R. S. Muller. Piezoelectric microphone with on-chip cmos circuits. *Journal Microelectromechanical Systems*, 2:111–120, September 1993.

[11] R. Kressman, G. Hess, and R. Schellin. New results of micromachined silicon subminiature microphones using piezoelectric polymer layers. *9th International Symposium on Electrets*, pages 1044–1049, 1996.

[12] R. Schellin, G. Hess, W. Kuehnel, G. M. Sessler, and E. Fukada. Silicon subminiature microphones with organic piezoelectric layers - fabrication and acoustical behavior. *Ieee Transactions on Electrical Insulation*, 27(4):867–871, AUG 1992.

[13] J. Franz. Funktionsweise und technishe realisierung eines piezoelektrischen siliziumsensors fur akustiche grossen. *VDI-Berichte*, 677:299–302, 1988.

[14] Lawrence E. Kinsler and Austin R. Frey. *Fundamentals of acoustics*. Wiley, New York, 1982.

[15] F. A. Levinzon. Fundamental noise limit of piezoelectric accelerometer. *Ieee Sensors Journal*, 4(1):108–111, FEB 2004.

[16] B. A. Auld. *Acoustic Fields and Waves in Solids*. Krieger, 1973.

[17] R. Herdier, D. Jenkins, D. Remiens, M. Dupont, and D. Osmont. A silicon cantilever beam structure for the evaluation of d_{31}, d_{33} and e_{31} piezoelectric coefficients of pzt thin films. *16th IEEE International Symposium on Applications of Ferroelectrics*, pages 725–727, May 2007.

[18] Ieee standard on piezoelectricity. Technical report, 1987.

[19] Q. M. Wang and L. E. Cross. Performance analysis of piezoelectric cantilever bending actuators. *Ferroelectrics*, 215:187–213, March 1998.

[20] C. K. Lee. Theory of laminated piezoelectric plates for the design of distributed sensors/ actuators. part i: Governing equations and reciprocal relationships. *Journal of the Acoustical Society of America*, 87:1144–1158, March 1990.

[21] H. F. Tiersten. *Linear Piezoelectric Plate Vibration*. Plenum, 1969.

[22] T. L. Ren, L. T. Zhang, H. S. Liu, L. T. Liu, and Z. H. Li. A novel ferroelectric based microphone. *Microelectronic Engineering*, 66(1-4):683–687, APR 2003.

[23] R. S. Fazzio, T. Lamers, O. Buccafusca, A. Goel, and W. Dauksher. Design and performance of aluminum nitride piezoelectric microphones. *14th International Conference on Solid-State Sensors, Actuators and Microsystems*, pages U632–U633, June 2007.

[24] M. S. Weinberg. Working equations for piezoelectric actuators and sensors. *IEEE Journal of Microelectromechanical Systems*, 8:529–533, December 1999.

[25] D. Devoe and A. P. Pisano. Modeling and optimal design of piezoelectric cantilever microactuators. *IEEE Journal of Microelectromechanical Systems*, 6:266–270, September 1997.

[26] M. Krommer. On the correction of the bernoulli-euler beam theory for smart piezoelectric beams. *Journal of Smart Materials and Structures*, 10:668–680, 2001.

[27] M. Krommer and H Irschik. On the influence of the electric field on free transverse vibrations of smart beams. *Journal Smart Materials and Structures*, 8:401–410, 1999.

[28] E. Elka, D. Elata, and H. Abramovich. The electromechanical response of multilayered piezoelectric structures. *IEEE Journal of Microelectromechanical Systems*, 13:332–341, April 2004.

[29] P. V. Loeppert and B. Zinserling. Silicon microphone for high volume consumer electronic applications. *Fortschritte Der Akustik*, 31:393–394, 2005.

[30] H. F. Tiersten. Electroelastic equations for electroded thin plates subject to large driving voltages. *Journal of Applied Physics*, 74:3389–3393, September 1993.

[31] Q. M. Wang, Q. Zhang, B. Xu, R. Liu, and L. E. Cross. Nonlinear piezoelectric behavior of ceramic bending mode actuators under strong electric fields. *Journal of Applied Physics*, 86:3352–3360, 1999.

[32] K. Shimada, T. Sota, K. Suzuki, and H. Okumura. First-principles study of piezoelectric constants in strained bn, aln, and gan. *Japneese Journal of Applied Physics*, 37:1421–1423, 1998.

[33] S. N. Mahmoodi, M. F. Daqaq, and N. Jalili. On the nonlinear-flexural response of piezoelectrically driven microcantilever sensors. *Sensors and Actuators A*, 153:171–179, 2009.

[34] S. Braun, D. J. Ewins, and S. S. Rao. *Eneyclopedia of vibration.* Academic Press, San Diego, 2002.

[35] G. Piazza. *Piezoelectric Aluminum Nitride Vibrating RF MEMS for Radio Front-End Technology.* PhD thesis, University of California Berkeley, 2005.

[36] S. Trolier-McKinstry and P. Muralt. Thin film piezoelectrics for mems. *Journal of Electroceramics*, 12(1-2):7–17, JAN-MAR 2004.

[37] P. L. Chen, R. S. Muller, R. M. White, and R. Jolly. Thin film zno-mos transducer with virtually dc response. *Ultrasonics Symosium*, pages 945–948, 1980.

[38] P. Soussan, K. O'Donnell, J. D'Haen, G. Vanhoyland, E. Beyne, and H. A. C. Tilmans. Pulsed dc sputtered aluminum nitride: A novel approach to control stress and c-axis orientation. *Matr.Res.Soc.Symp.Proc.*, 833:G2.2.1–G2.2.6, 2005.

[39] G. Carlotti, G. Socino, A. Petri, and E. Verona. Acoustic investigation of the elastic properties of zno films. *Applied Physics Letters*, 51:1889–1891, December 1987.

[40] K. Tsubouchi and N. Mikoshiba. Zero-temperature-coefficient saw devices on aln epitaxial films. *IEEE Transactions on Sonics and Ultrasonics*, 32:634–644, September 1985.

[41] P. Delobelle, E. Fribourg-Blanc, and D. Remiens. Mechanical properties determined by nanoindentation tests of $[pb(zr,ti)o_3]$ and $[pb(mg_{1/3}nb_{2/3})_{1-x}ti_xo_3]$ sputtered thin films. *Thin Solid Films*, 515:1385–1393, 2006.

[42] M. A. Dubois and P. Muralt. Measurement of the effective transverse piezoelectric coefficient e(31,f) of aln and pb(zr-x,ti1-x)o-3 thin films. *Sensors and Actuators A-Physical*, 77(2):106–112, OCT 12 1999.

[43] J. Bergqvist and F. Rudolf. A silicon condenser microphone using bond and etch-back technology. *Sensors and Actuators A*, 45:115–124, 1994.

[44] R. P. Ried, E. S. Kim, D. M. Hong, and R. S. Muller. Piezoelectric microphone with on-chip cmos circuits. *IEEE Journal of Microelectromechanical Systems*, 2(3):111–120, SEPT 1993.

[45] F. A. Levinzon. Noise of the jfet amplifier. *IEEE Transactions on Circuits and Systems*, 47:981–985, 2000.

[46] F. P. Mechel. Notes on the radiation impedance, especially of piston-like radiators. *Journal of Sound and Vibration*, 123:537–572, October 1987.

[47] W. E. Newell. Miniaturization of tuning forks. *Science*, 161:1320–1326, September 1968.

[48] M. Ahmad. A simple scheme for loss angle measurement of a capacitor. *IEEE Transactions on Energy Conversion*, 19:228–229, March 2004.

[49] Namba. Resistivity and temperature coefficient of thin metal films with rough surface. *Japanese Journal of Applied Physics*, 9(11):1326, 1970.

[50] P. R. Gray and R. G. Meyer. *Analysis and Design of Analog Integrated Circuits*. Wiley, 3 edition, 1993.

[51] Stephen Timoshenko and S. Woinowsky-Krieger. *Theory of plates and shells*. McGraw-Hill, New York, 1959.

[52] M. Yu and B. Balachandran. Sensor diaphragm under initial tension: Linear analysis. *Experimental Mechanics*, 45(2):123–129, APR 2005.

[53] G. F. Iriarte, J. Bjurstrom, J. Westlinder, F. Engelmark, and I. V. Katardjiev. Synthesis of c-axis-oriented aln thin films on high-conducting layers: Al, mo, ti, tin, and ni. *IEEE Transactions On Ultrasonics, Ferroelectrics and Frequency Control*, 52:1170–1174, July 2005.

[54] F. Martin, P. Muralt, M.A. Dubois, and A. Pezous. Thickness dependence of the properties of highly c-axis textured aln thin films. *Journal of Vacuum Science & Technology A*, 22(2):361–365, March 2004.

[55] F. Martin, P. Muralt, and M.A. Dubois. Process optimization for the sputter deposition of molybdenum thin films as electrode for aln thin films. *Journal of Vacuum Science & Technology A*, 24(4):946–952, July 2006.

[56] J. Gupta. A comparative study of stress, resistivity and microstructure in copper and copper-alloy thin films. Master's thesis, Massachusetts Institute of Technology, 1992.

[57] S. Mishin, D. R. Marx, B. Sylvia, V. Lughi, K. L. Turner, and D. R. Clark. Sputtered aln thin films on si and electrodes for mems resonators: Relationship between surface quality microstructure and film properties. *IEEE Ultrasonics Symposium*, pages 2028 – 2032, 2003.

[58] Z. Wang, Q. Zhang, and H. Feng. High performance silicon condenser microphone with perforated single crystal silicon backplate. United States Patent 7,132,307, November 2006.

[59] Scott Alan Smith. *Inductively Coupled Plasma Etching of III-N Semiconductors*. PhD thesis, North Carolina State University, 1999.